MorphingSkin: A Skin-like Platform that Integrates Multimodal Hydraulic Actuators Based on Flexible Electroosmotic Pumps

Tianyu Yu
Morphing Matter Lab
University of California, Berkeley
Berkeley, California, USA
tianyuyu@berkeley.edu

Peisheng He
University of California, Berkeley
Berkeley, California, USA
hopsonhe@berkeley.edu

Bob Tianqi Wei
College of Engineering
University of California, Berkeley
Berkeley, California, USA
bobtianqiwei@berkeley.edu

Chenyuheng Wang
Tsinghua University
Beijing, China
wcyh23@mails.tsinghua.edu.cn

Xueqing Li
Tsinghua university
Beijing, Beijing, China
li-xq23@mails.tsinghua.edu.cn

Xuezhu Wang
Tsinghua University
Beijing, China
15626222995@163.com

Yao Lu
Tsinghua University
Beijing, China
lainaluyao@gmail.com

Wei Yue
University of California, Berkeley
Berkeley, California, USA
wei_yue@berkeley.edu

Megan Teng
University of California, Berkeley
Berkeley, California, USA
meganteng@berkeley.edu

Zihan Wang
Department of Mechanical Engineering
University of California, Berkeley
Berkeley, California, USA
zihan.wang@berkeley.edu

Liwei Lin
Mechanical Engineering
University of California, Berkeley
Berkeley, California, USA
lwlin@berkeley.edu

Haipeng Mi
Tsinghua University
Beijing, China
mhp@tsinghua.edu.cn

Qi Lu
The Future Laboratory
Tsinghua University
Beijing, China
luq@mail.tsinghua.edu.cn

Lining Yao*
Mechanical Engineering, Morphing Matter Lab
University of California, Berkeley
Berkeley, California, USA
liningy@berkeley.edu

Abstract

Interactive surfaces have garnered significant attention in Human-Computer Interaction, with fluid-driven actuators being a promising actuation technology due to their flexible form factors and multimodal interactivities. However, traditional fluid-driven systems typically rely on bulky and noisy electromechanical hardware, limiting their portability and practicality. While recent work has introduced compact hydraulic actuators like electroosmotic pumps (EOPs) in haptic devices, their potential for building multifunctional interactive surfaces remains largely unexplored.

In this work, we present MorphingSkin, a skin-like platform that integrates multiple, multimodal hydraulic actuators using flexible EOPs as lightweight and self-contained fluidic actuators. We introduce the architecture of MorphingSkin and its versatile design space for multimodal actuation in force, shape, optical, and weight domains. We demonstrate interactive and robotic applications that integrate multiple actuators working collectively within a single MorphingSkin device. Through this work, we envision the future of using MorphingSkin technology for interactive surfaces that integrate flexible form factors and multimodal actuation capabilities.

CCS Concepts

• **Human-centered computing** → **Interaction devices**; **Interactive systems and tools**; • **Hardware** → *Sensors and actuators*; *Electro-mechanical devices*; Emerging technologies.

Keywords

Interactive surface, Multimodal actuators, Fluid-driven interfaces, Electroosmotic pumps, Smart wearables, Robotics, Tangible display

ACM Reference Format:
Tianyu Yu, Peisheng He, Bob Tianqi Wei, Chenyuheng Wang, Xueqing Li, Xuezhu Wang, Yao Lu, Wei Yue, Megan Teng, Zihan Wang, Liwei Lin,

*Corresponding author.

This work is licensed under a Creative Commons Attribution 4.0 International License.

UIST '25, Busan, Republic of Korea

© 2025 Copyright held by the owner/author(s).

ACM ISBN 979-8-4007-2037-6/25/09
https://doi.org/10.1145/3746059.3747685

Haipeng Mi, Qi Lu, and Lining Yao. 2025. MorphingSkin: A Skin-like Platform that Integrates Multimodal Hydraulic Actuators Based on Flexible Electroosmotic Pumps. In *The 38th Annual ACM Symposium on User Interface Software and Technology (UIST '25), September 28–October 01, 2025, Busan, Republic of Korea.* ACM, New York, NY, USA, 21 pages. https://doi.org/10.1145/3746059.3747685

1 Introduction

Interactive surfaces have garnered significant attention within the field of Human-Computer Interaction (HCI), which are capable of providing multimodal physical interactions on object surfaces and human bodies for a wide range of applications, such as tangible displays [24], haptic wearables [10], and robotic interfaces [8]. Among the various technologies employed to realize interactive surfaces, fluid-driven actuators (i.e., pneumatic and hydraulic actuators) have attracted increasing interest due to their distinctive advantages. The inherent fluidity of the working medium allows such interfaces to conform to complex geometries [35] or adapt to flexible, reconfigurable shapes [44]. In addition, the flowing behavior of the working material enables dynamic transformations of various physical properties on object surfaces, such as color [42], shape [66], temperature [72], and weight [43], as different interaction modalities.

Despite these benefits, traditional approaches to actuating and controlling fluid-driven systems typically rely on bulky and noisy electromechanical pumps and valves, which limits the possibility for portable and practical designs [35, 66, 72]. In response to these challenges, recent research in the domain of hydraulic actuators has explored the usage of lightweight and self-contained fluidic actuators that are capable of eliminating the usage of rigid, mechanical moving parts [5, 49]. These fluidic systems are mostly driven by high-voltage power sources, eliminating the need for mechanical pumps. Among these advanced hydraulic actuators, electroosmotic pumps (EOPs) stand out for their compact multilayered structures that generate electrokinetic flow directly in response to voltage signals, typically below 1kV [70]. Although prior work has explored utilizing EOPs to develop shape-changing actuators for haptic button [48], display [55], and gloves [53], we see an underexplored opportunity to expand the usage of EOPs beyond rigid, panel-based displays, toward supporting richer interaction modalities and functionalities highlighted by the fluidic-driven actuators.

In this work, we present MorphingSkin, a skin-like platform that integrates multiple, multimodal hydraulic actuation using flexible EOPs as lightweight, self-contained fluidic actuators. We introduce the overall architecture of MorphingSkin, including the flexible EOPs and the surrounding elastomeric structures, which together span a versatile design space for multimodal actuation in force, shape, optical, and weight domains. We next demonstrate a wide range of applications using MorphingSkin as an interactive surface in robotics, wearables, and physical interaction contexts, each utilizing multiple actuators that work collectively within a single MorphingSkin device. We then detail the fabrication process for MorphingSkin devices with customized shapes and both flexible and partially stretchable form factors, along with a portable driving hardware system that enables untethered operation. Lastly, we present technical evaluations of the MorphingSkin system, which show comparable hydraulic performance to prior work. Through this work, we envision the future of using MorphingSkin technology for interactive surfaces that integrate flexible form factors and multimodal actuation capabilities.

2 Related Work

2.1 Interactive surfaces and skins

Interactive surfaces have been a widely explored topic in HCI, which embed multimodal physical actuation or sensing capabilities on the surfaces of everyday objects or the human body. Among these, interfaces that feature thin, flexible, or untethered form factors allow themselves to conform seamlessly to various surfaces, further extending their potential as a universal, interactive second skin.

For instance, on object surfaces, researchers have explored attaching shape-changing devices to enable a wide range of applications, including haptic feedback [7, 9], information communication [8], kinetic motion [65], or modulation of the physical environment such as illumination control [1, 14, 22]. Other work has focused on adding color-changing materials on object surfaces to alter the physical appearance [27, 52] or display dynamic information [21, 51]. Additionally, some approaches embedded flexible electronics on object surfaces to support diverse sensing capabilities, such as touch sensing [16], object recognition [63], or gesture and activity recognition [57].

Similarly, on human skin, various approaches have been studied for embedding multimodal interactions. For example, previous work has introduced wearable devices that provide force output [10, 39], electrical stimulation [59, 62], texture changes [20], thermal feedback [19, 46], or friction modulation [41], offering rich multimodal haptic experiences. Other research has utilized color-changing or shape-changing materials to create wearable artifacts or on-skin displays for different types of functional appearance, such as information encoding [25, 33], humidity regulation [67], or personalized expression [12, 30, 32, 56]. Furthermore, extensive research has focused on integrating electronics with textiles to realize sensing capabilities, such as posture tracking [73–75] and physiological sensing [40], to enable smart wearables.

Our work builds upon these prior works by introducing a new approach to develop a flexible, skin-like platform that integrates multimodal actuation capabilities.

2.2 Fluid-driven actuation

Among the various technologies to realize interactive surfaces, fluid-driven actuators (i.e., pneumatic and hydraulic actuators) have garnered increasing attention due to their distinctive advantages. Firstly, the inherent fluidity of the working medium allows these interfaces to adapt to complex, flexible, and reconfigurable geometries, making them well-suited for applications on complex object surfaces [45] or the human body [36].

More importantly, the flowing behavior of the working fluid enables dynamic transformations of a range of physical properties that serve as the foundation for multimodal actuation. For instance, extensive work has utilized pneumatic actuators [23, 31, 38, 66, 71] and hydraulic actuators [7, 64] in different designs to achieve shape- or texture-changing surfaces. Other work has explored controlling the colored fluid distribution [2, 35, 42, 58] or modulating the fluid

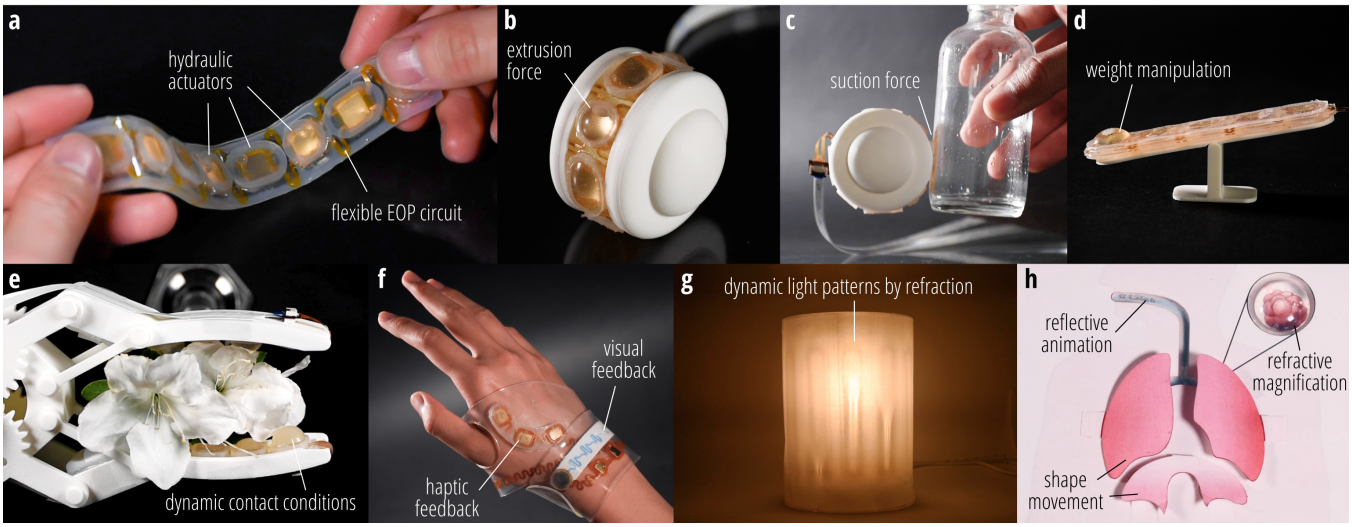

Figure 1: MorphingSkin. A skin-like platform that integrates multiple hydraulic actuators based on flexible electroosmotic pumps, providing multimodal actuation capabilities, spanning force, shape, optical, and weight domains, which enables a wide range of applications, including actuating surfaces on (b-c) companion robots and (e) gripper fingers, (f) multimodal wearables, and physical interaction contexts such as (g) dynamic lampshades and (h) tangible displays.

transparency [26] to enable dynamic visual appearance on 3D objects. In addition, works such as MobileGravity [28], PumpVR [29], and See-Saw [43] utilize liquid mass transfer to alter weight distribution for haptic feedback in VR experiences or physical kinetic installations. Thermotion [72], Thermaterial [69], and Therminator [17] use fluids as thermal media to program surface temperature or deliver dynamic thermal haptic feedback. Chemical Haptics [37], Logic Bonbon [11], and Taste Retargeting [3] utilize fluids as chemical carriers, providing multimodal haptic or gustatory feedback on the human body.

Inspired by these prior works, our work explores integrating multiple types of hydraulic actuators into interactive surfaces to achieve flexible form factors and multimodal actuation capabilities.

2.3 Electrical-hydraulic actuators

Traditional approaches to actuating and controlling fluid-driven systems often rely on bulky and noisy electromechanical pumps and valves, which limits their feasibility in portable or practical applications [66, 72]. Research in pneumatic systems has pursued multiple approaches for lightweight actuation solutions [15, 54]. Similarly, recent advances in hydraulic actuators have also focused on building compact, self-contained actuators to eliminate rigid mechanical moving parts.

One type of technology is Hydraulically Amplified Self-Healing Electrostatic (HASEL) actuators, which couple electrostatic and hydraulic forces to support a variety of actuation modes [49]. These actuators have been widely used in building haptic displays [7, 13, 34, 50] and robots [4, 47, 68] for their fast and remarkable force output. Another branch involves Electrohydrodynamic (EHD) actuators, which generate continuous electrokinetic flow with dielectric fluids based on electrochemical reactions under high electric fields [5]. Researchers have employed EHD actuators to create modular toolkits [44], dynamic displays [2, 26], as well as soft robots [60]. However, the aforementioned actuators typically require high-voltage power supplies (500V–10kV) or lack the compactness for integration within thin, skin-like platforms.

In contrast, Electroosmotic Pumps (EOPs) stand out for their compact, multilayered structure capable of generating electrokinetic flow under relatively low voltages (typically <1kV) based on the intrinsic electrical double layer. In the HCI field, Shultz et al. [55] utilized EOPs to develop thin-panel displays that integrate an array of shape-changing actuators for haptic feedback. Shen et al. [53] used EOPs in miniature designs to create lightweight, high-resolution shape-changing fingertip arrays for multi-type tactile experiences in VR applications. Rae-Grant et al. [48] developed dynamic tactile buttons based on EOPs that provide fast response and closed-loop deformation control.

While EOPs have demonstrated potential in haptic interfaces, we see an underexplored opportunity to expand the usage of EOPs beyond rigid, panel-based displays, toward supporting richer interaction modalities and functionalities highlighted by the fluidic-driven systems.

In this work, we present MorphingSkin, a skin-like platform that utilizes flexible EOPs as lightweight, self-contained hydraulic actuators, integrating multiple, multimodal hydraulic actuation.

3 MorphingSkin Mechanism

To apply the EOP technique to our envisioned flexible and multimodal interface, a tailored structural composition is presented. In particular, the design consideration of the flexible EOP layer with the integrated flexible and partially stretchable EOP circuit is

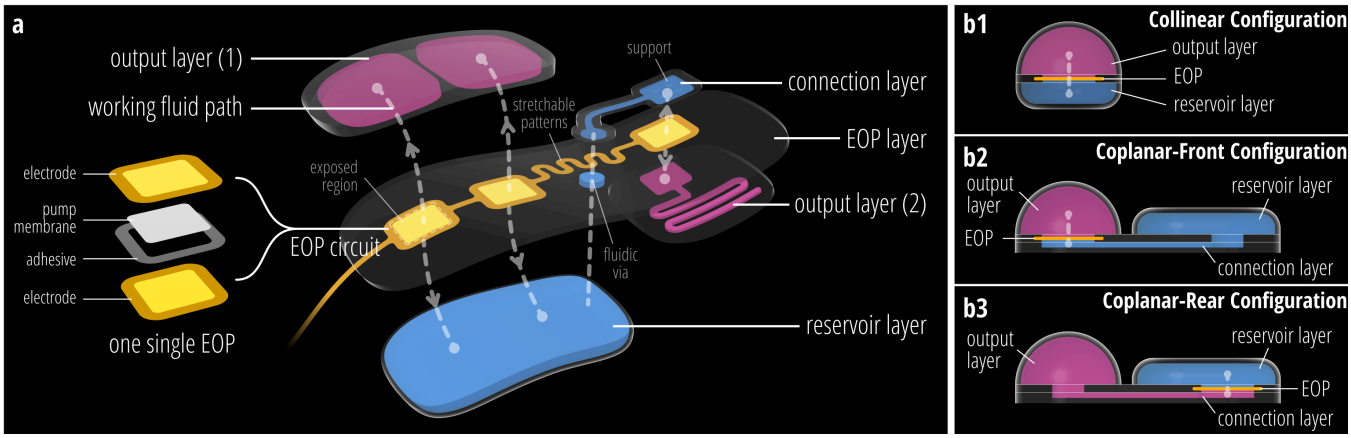

Figure 2: (a) MorphingSkin structure composition, including the coated EOP layer, output layer (colored in pink), reservoir layer (in blue), connection layer, and the working fluid path (by white dashed curves), all designed using flexible or stretchable materials and structures. (b) Three configurations of the working fluid path, including Collinear, Coplanar-Front, and Coplanar-Rear configurations.

unique to this project. In addition, we modularize essential functional components to allow design flexibility to customize the output modalities and form factors for different applications.

3.1 Structure composition

In this section, we introduce the structure composition of MorphingSkin. As shown in Figure 2a, the MorphingSkin structure is centered around a middle EOP layer, which integrates multiple independently controlled EOP units. Various types of elastic shells are attached to both sides of the EOP layer, functioning as output layers, reservoir layers, or connection layers, and enclosing the working fluid inside that serves as the actuation medium. The entire skin is designed using flexible or stretchable materials and structures. We detail the key structural components below:

The EOP circuit is the embedded electronic circuit containing multiple EOP units, each of which follows the basic structure consistent with prior work [48, 55, 70], consisting of two face-to-face mesh-patterned electrodes that sandwich a pumping membrane and an adhesive layer, as shown in Figure 2a. The two electrodes are individually routed to the connector on their respective circuit boards, enabling independent voltage control across each electrode pair. In this work, we employ flexible printed circuits (FPCs) as the base circuit board and use stretchable interconnect patterns to provide overall flexibility and partial stretchability to the system. The pumping membrane serves as the substrate in contact with the working fluid, collectively forming the intrinsic electric double layer to produce the electroosmotic flow under applied electric fields. The adhesive layer ensures bonding and sealing between the paired electrodes. The detailed design parameters for the EOP circuit are presented in Section 6.1.1. During operation, each EOP can be independently actuated by applying voltage, pumping the working fluid to either side.

The EOP layer consists of the EOP circuit coated with stretchable materials, forming the structural backbone of MorphingSkin, as shown in Figure 2a. This layer also serves as a continuous barrier that separates the elastic shells on both sides of the device, while the electrode mesh regions remain exposed to allow working fluid to pass through. When needed, additional fluidic vias are designed to facilitate cross-layer fluid transport.

The output layer is a type of elastic shell attached to the EOP layer, designed to provide functional actuations when the working fluid is pumped into or out of the shell through the embedded EOPs. By varying the shell geometry (e.g., volumetric cavities or fluidic channels, shown in Figure 2a), as well as the material stiffness and transparency, the output layer enables a variety of actuation modalities (e.g., force generation, shape changes, or optical changes). The design space of these multimodal actuation is detailed in Section 4.

The reservoir layer is another type of elastic shell attached to the EOP layer, designed to store and supply working fluid for the EOPs in the MorphingSkin device. Typically, the reservoir layers are composed of soft, sagging elastic bags that passively deform to balance the internal pressure with the atmospheric pressure during fluid transport. Note that multiple EOPs may share a common reservoir layer to save space and the working fluid, as shown in Figure 2a.

The connection layer is a thin, planar elastic shell engraved with millifluidic channels, enabling in-plane fluid transfer on either side of the skin. Each fluidic channel terminates at either an exposed electrode region or a fluidic via on the EOP layer, connecting the EOPs and the elastic shells on different locations, as shown in Figure 2a. To prevent flow blockage when the internal pressure decreases, small structural supports are added on the wall opposite to EOP electrodes to ensure enough spacing for fluid transport.

The working fluid functions as the fluidic medium for actuation throughout MorphingSkin. It is typically distributed within the elastic shells and remains in contact with the embedded EOPs via the exposed region on the EOP layer. When voltage is applied to an EOP, the working fluid is then transferred across the EOP, enabling functional actuation.

In addition, the presented structure is compatible with the integration of other functional electronic components, such as the heart rate sensors and touch buttons shown in the later application section.

3.2 Hydraulic actuator and working fluid path

In the complete MorphingSkin system, each EOP is connected to one output layer and one reservoir layer through either side (an intermediate connection layer may be used for fluidic routing). During operation, the EOP pumps the working fluid either from the reservoir layer to the output layer or in the reverse direction, which in turn alters the fluid mass, as well as the hydraulic pressure within the output layer, resulting in pre-programmed functions such as shape changes. Thus, each EOP, together with its adjoining output layers and reservoir layers, constitutes an individual *hydraulic actuator* within the MorphingSkin.

Specifically, when the EOP is applied with a voltage that pumps the working fluid into the output layer, the fluid mass within the output layer increases, and the hydraulic pressure tends to rise to a *positive pressure* relative to the atmospheric pressure. When the voltage is reversed, the EOP then pumps the working fluid back into the reservoir layer, decreasing the fluid mass in the output layer and thereby tending to create a *negative pressure* within the output layer. These positive and negative hydraulic pressures serve as the active driving force for the activation and deactivation of each actuator. When no voltage is applied, the EOP enters a *high-resistance state*, during which the working fluid can transfer across the EOP under high fluidic resistance, gradually balancing the pressure between the two sides.

Within each actuator, the output layer, EOP, and reservoir layer are connected in sequence, forming a continuous, reversible, and bidirectional *working fluid path*. Based on the spatial arrangement of these components, we classify the fluidic paths into three configurations, as shown in Figure 2b:

(1) **Collinear configuration:** The output layer, EOP, and reservoir layer overlap vertically (Figure 2b1). This design is structurally compact and easy to fabricate, but may result in a larger overall thickness.
(2) **Coplanar-Front configuration:** The output and reservoir layers are located on the same side of the EOP layer, while the EOP is covered within the output layer region and connected to the reservoir via a connection layer through the back side (Figure 2b2). This layout is well-suited for saving vertical space, especially when the reservoirs can be arranged laterally alongside the output layer.
(3) **Coplanar-Rear configuration:** This configuration is similar to the Coplanar-Front configuration, but with the EOP covered within the reservoir region (Figure 2b3). The layout allows greater design freedom in the positioning and geometry of the output layer, e.g., routing it to an area not obstructed by the EOP circuit via a connection layer. However, the expected hydraulic pressure changes in the output layer may be weakened due to the self-cushioning or fluidic resistance introduced by the connection layer.

4 Multimodal Actuation Design Space

By varying the design of the multilayer structures, MorphingSkin achieves a versatile design space for multimodal actuation, spanning force, shape, optical, and weight domains. In this section, we detail the structure design and the actuation behavior of each actuation modality. Note that, unless otherwise specified, all demonstrations in this section were conducted at a driving voltage of ±250 V. Details of the driving hardware system are provided in Section 6.2.

4.1 Force generation

Even though extrusion and suction through EOP have been introduced in literature [48, 55], here we performed our own experiments to see if such functions are compatible with the flexible EOP layer and quantify the resulting forces in our proposed structure composition.

4.1.1 Extrusion. The extrusion modality employs an output layer that remains flat in its static state (Figure 3a1). Upon activation, the embedded EOP transfers working fluid from the reservoir layer into the output layer, leading to an increase in both the volume and internal hydraulic pressure of the output layer. When there is no external load, the rising hydraulic pressure causes the output layer to deform into a dome-like shape (Figure 3a2). When a load is present, the output layer functions as a force transmission medium, applying an extrusion force to the object it is in contact with. For instance, Figure 3a3-4 demonstrates the actuator lifting a 100-gram weight.

4.1.2 Suction. The suction modality employs a bowl-shaped output layer that contains a cavity holding a certain volume of working fluid in the static state (Figure 3b1). During activation, the embedded EOP pumps the working fluid from the output layer back into the reservoir layer, resulting in a reduction in both volume and internal hydraulic pressure within the output layer. This leads to an inward deformation of the output layer in the absence of load, as shown (Figure 3b2), while enabling it to generate a suction force when in airtight contact with an object surface. As shown in Figure 3b3-4, the actuator is able to apply a suction force to a 100-gram weight, suspending it in mid-air.

4.2 Shape output

4.2.1 Kinematic Motion. The kinematic motion is built based on the extrusion modality, wherein the actuator is integrated into a kinematic structure. Upon activation, the generated extrusion force is harnessed to drive the movement of the kinematic system. Figure 3c illustrates the opening motion of a kinematic hinge within 0.54 seconds, driven by an actuator positioned near the pivot point.

4.2.2 Kirigami Surface. The kirigami surface modality is also based on the extrusion modality. However, it leverages the deformation of the output layer to induce texture changes on an overlying kirigami surface as it undergoes out-of-plane deformation along with the output layer. Figure 3d illustrates the shape change of an auxetic surface, laser-cut from copy paper and adhered to the output layer. During activation, the entire kirigami surface conforms to the dome-like shape of the output layer, with regions near the center adaptively opening to accommodate the deformation.

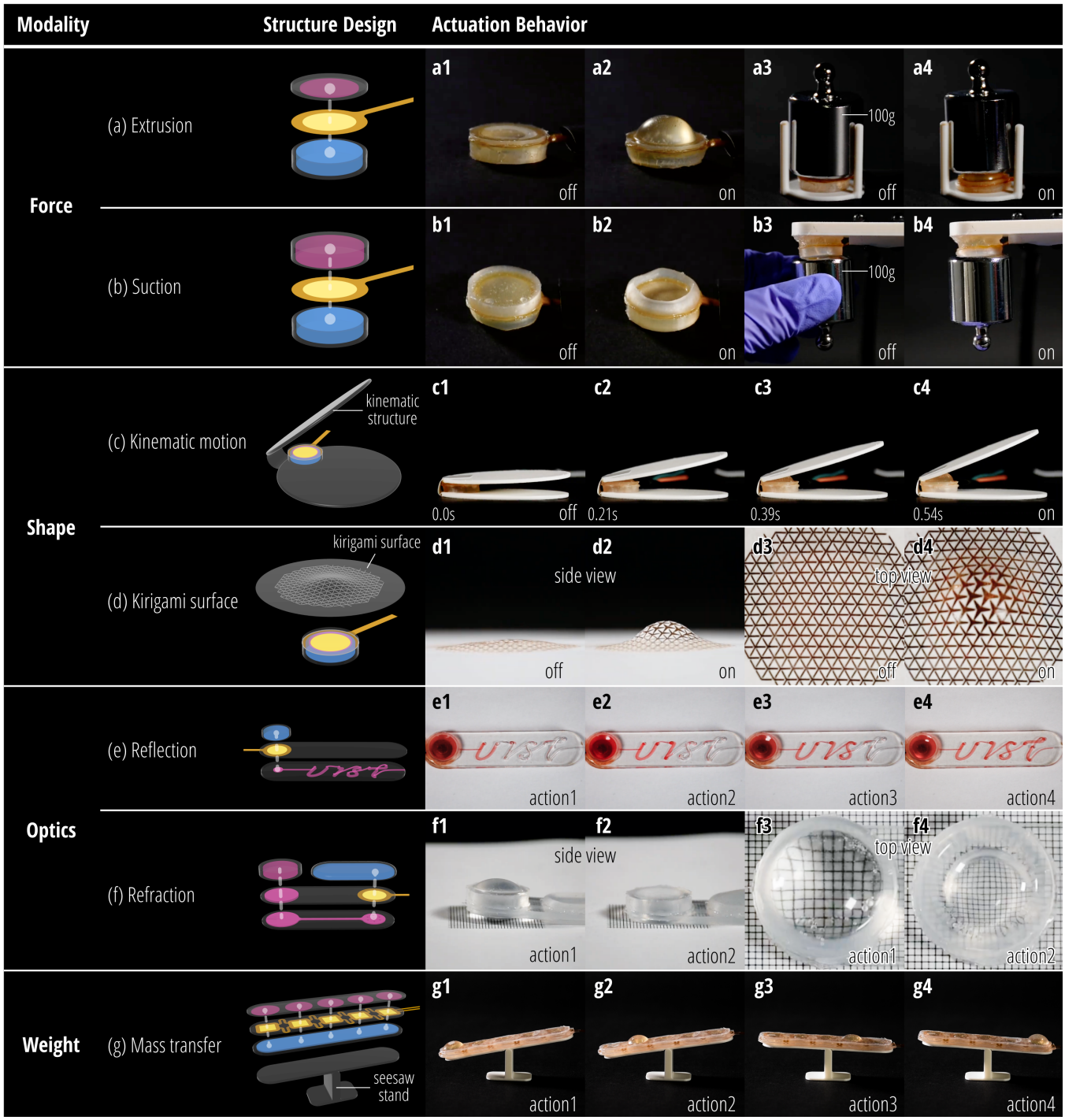

Figure 3: Design space of multimodal actuation by MorphingSkin, spanning force, shape, optical, and weight domains. Each modality is detailed with the 3D models of the structure design (follows the color code in Figure 2a) and the photographs of the actuation behaviors.

4.3 Dynamic optics

4.3.1 Reflection. The reflection modality leverages the flow behavior of the colored working fluid within the fluidic channels embedded in the transparent output layer. Figure 3e presents four distinct actions achieved by the actuator, in which the output layer incorporates multilayer fluidic channels [42] that sequentially display the characters 'U', 'I', 'S', and 'T'. This actuation enables changes in the reflective optical appearance of a material surface, which, in contrast to light-emitting displays (e.g., LEDs), may provide a more tangible and ambient form of visual feedback. For all the reflective actuations designed throughout this paper, the actuation voltage is set to ±50 V to achieve an appropriate flow rate for the animation. Notably, the output layer in this case can also remain open to the atmosphere to balance internal pressure, allowing the fluid distribution, as well as the visual pattern, to be preserved even after the power is turned off.

4.3.2 Refraction. The refraction modality employs a transparent output layer filled with working fluid as the refractive medium. As the embedded EOP pumps fluid into or retracts it from the output layer, the internal pressure changes accordingly, thereby altering both the shape and the optical refractive properties of the output layer, functioning as a dynamic soft lens. For example, Figure 3f illustrates a circular output layer undergoing inflation and deflation activation, resulting in a shape transition between convex (Figure 3f1) and concave (Figure 3f2) lens profiles, thus producing magnification (Figure 3f3) and minification (Figure 3f4), respectively. In this case, the refraction actuator adopts a Coplanar-Rear Configuration introduced in Section 3.2, where the EOP circuit is positioned away from the output layer to prevent blocking the light from passing through.

4.4 Weight manipulation

The weight manipulation in MorphingSkin relies on the mass transfer of the working fluid across the device, driven by the embedded EOPs during activation. For instance, Figure 3g1–4 illustrate a MorphingSkin device comprising five separate output layers connected to a shared reservoir. By selectively pumping the working fluid into different output layers, the center of mass shifts accordingly, causing the seesaw stand to tilt at different angles.

5 Example Applications

In this section, we focus on applications that highlight the unique qualities of MorphingSkin, including its skin-like thin form factor, flexibility, conformability, multimodal capabilities, and high customizability. We demonstrate how MorphingSkin can augment existing rigid surfaces—for example, by enabling a rigid gripper with tunable surface textures and contact conditions, or by serving as a conformal actuating surface for a companion desktop robot. MorphingSkin is also well suited for on-skin input/output interfaces. In addition, we explore its use in everyday physical interaction contexts, such as enhancing a tangible interface with dynamic multimodal displays and using its dynamic lens to manipulate the optical effects of a lamp. The control and driving hardware of these demonstrations are detailed in Section 6.2.

5.1 Dynamic contact conditions for robot skin

We first demonstrate the application of MorphingSkin as a functional skin for robots with dynamic contact conditions. We prototype a clamp-shaped gripper with two fingers, where the inner surface of each finger is embedded with a piece of MorphingSkin mounted against a rigid backbone, containing four linearly arranged actuators on each finger (Figure 4a). The actuators are implemented using a Coplanar-Front configuration, in which the reservoir is positioned laterally to reduce overall thickness while gaining structural support from the backbone. Each actuator can independently provide either extrusion, suction, or remain no actuation (Figure 4b), allowing the gripper to provide three distinct contact conditions: *soft contact*, *suction contact*, and *hard contact*, which match the mechanical sensitivities of diverse objects. We demonstrate the benefits in a familiar dining scenario that involves challenging items such as plates, cakes, and chocolates (Figure 4c).

Soft contact: For objects that are prone to deform under compression, such as cakes or decorative flowers, the actuators on the MorphingSkin can be selectively activated for extrusion, providing shape-adaptive, localized soft contact, e.g., on the planar sides of a cake (Figure 4d1) or the backside of flower petals (Figure 4e1). This allows the gripper to preserve the object's original shape as much as possible while maximizing contact area and providing sufficient contact pressure to lift the object by friction. In contrast, a conventional gripper with a fixed shape may forcibly squeeze the objects to obtain adequate contact, potentially causing unwanted deformation or damage, such as crushing the cake's corners (Figure 4d2) or distorting the entire flower (Figure 4e2).

Suction contact: For objects that are difficult to pinch, such as the top plate in a stack, or easily marred by gripping, such as delicate chocolates, the MorphingSkin actuators can apply suction contact under slight pressure for airtightness, allowing lifting forces to act outward, normal to the surface, and less invasive to the object. For example, Figure 4f1 shows the gripper lifting a piece of chocolate by suction contact at the fingertip, which helps avoid surface scratches that could result from direct gripping action. Figure 4f2 illustrates the lifting of the top plate in a stack through suction contact, which could otherwise be challenging for pinching manipulation.

Hard contact: For rigid and relatively heavy objects that require a larger gripping force, the MorphingSkin can operate in a passive mode with all actuators remaining inactive to provide hard contact. In this mode, the thin layer of the actuators above the finger's side wall is compressed, allowing the applied gripping force to be transmitted to the underlying rigid backbone, which provides firm support and sufficient contact pressure for lifting friction force. As shown in Figure 4g, the gripper lifts a square-shaped spice jar using hard contact between the four corners of the jar and the rigid surfaces of the finger backbone.

5.2 Desktop companion robots

Leveraging a mechanism similar to that of dynamic contact conditions, we then apply MorphingSkin to create a desktop companion robot with highly emotional expressiveness. As shown in Figure 5a-b, a wheel-shaped robot is equipped with circularly arranged actuators capable of both extrusion and suction actuation. As a

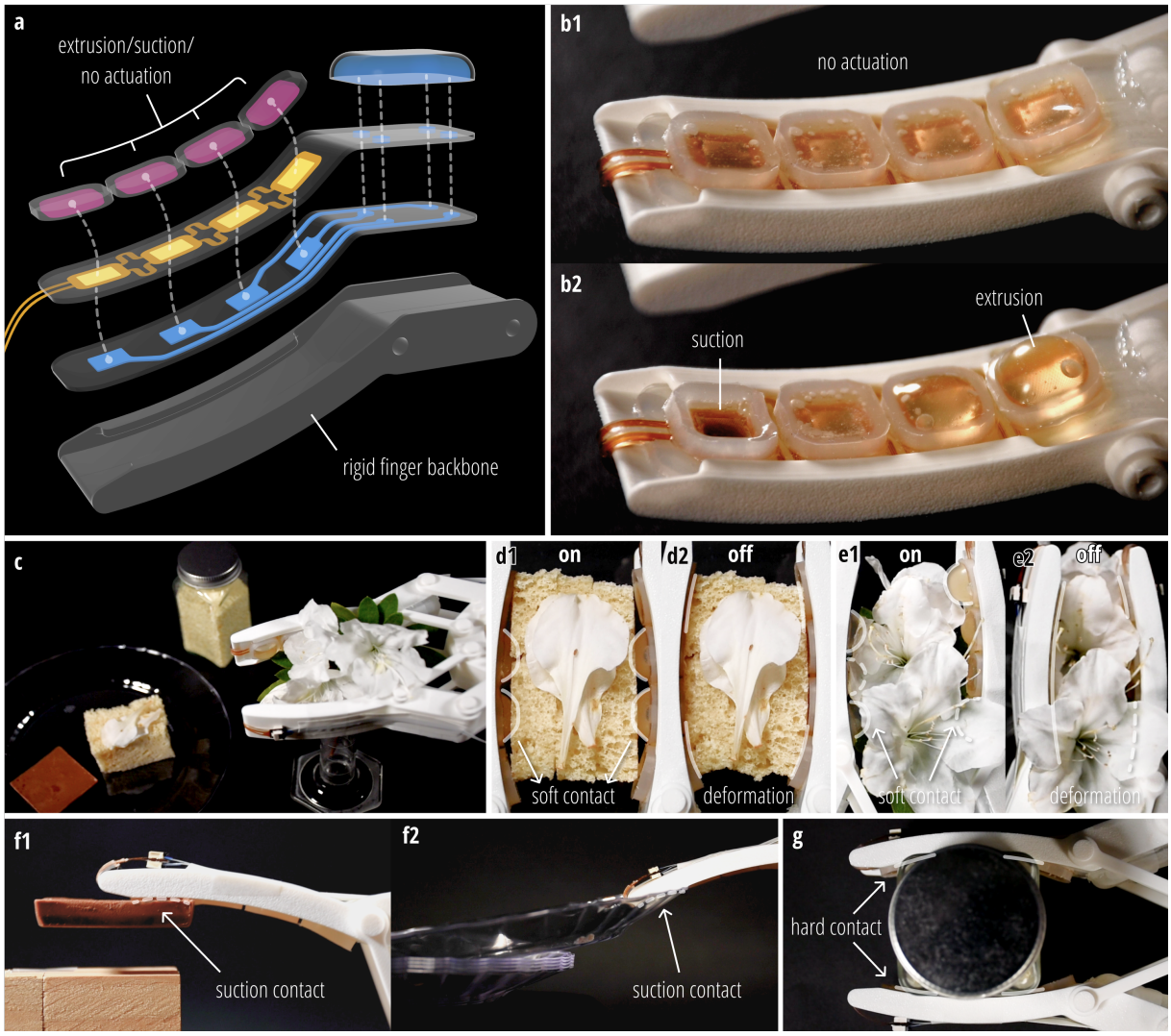

Figure 4: Application of MorphingSkin for robot skin with dynamic contact conditions. (a) The finger of a clamp-shaped gripper is embedded with MorphingSkin at the inner surface, (b) which provides extrusion, suction, or no actuation upon the four linearly arranged actuators. (c) The gripper provides different contact conditions to match the mechanical sensitivities of diverse objects, such as in a dining scenario, including (d-e) soft contact for objects that are prone to deform under compression, (f) suction contact for objects that are difficult to pinch or easily marred by gripping, and (g) hard contact for rigid and relatively heavy objects that require larger gripping force.

result, the collective actuation strategies can be mapped to a few distinct emotional expressions.

Calm emotion: This emotion is expressed when the robot periodically activates the exposed actuators to rapidly extrude and then gradually retract in a passive manner, simulating a rhythmic, breathing-like motion (Figure 5c1-3). During this period, users are invited to gently touch the MorphingSkin to experience the biomimetic and relaxing haptic sensations rendered on the robot's surface (Figure 5c4).

Frightened emotion: This emotion can be triggered by an unexpected physical touch or hit from the user (Figure 5d1). In response, the robot rapidly engages suction actuation across the entire ring of actuators, which simultaneously expresses a "defensive" posture (Figure 5d2) while producing an attachment behavior to the ground, mimicking the "freeze" response associated with fear. Once adhered to the ground, the robot remains in place even when gently poked by the user (Figure 5d3-4).

Excited emotion: This emotion is enabled by locomotion through cyclical extrusion actuation. The extrusion force generated by actuators in contact with the ground lifts the robot itself and induces a rolling motion to the side (Figure 5e2-3). This dynamic movement might be used to simulate an energetic or playful mood.

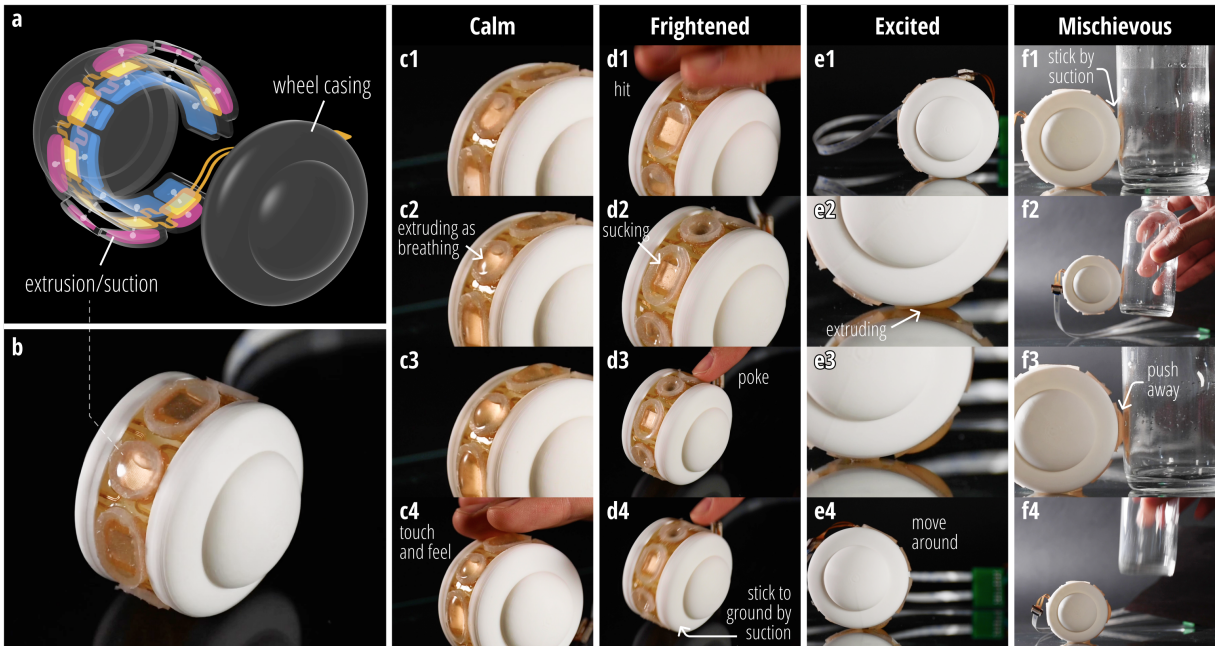

Figure 5: Application of MorphingSkin to create a desktop companion robot. (a) A desktop robot is designed using MorphingSkin as the body, containing circularly arranged actuators for extrusion and suction actuation. (b) Photograph of the desktop robot, which conveys highly expressive emotions, including (c) clam emotion based on periodical breathing-like extrusion actuation, (d) frightened emotion that engages suction actuation to express a "defensive" posture and "freeze" to the ground, (e) excited emotion based on locomotion by extrusion actuation, and (f) mischievous characteristic by interaction with surrounding objects.

Mischievous characteristic: This nuanced characteristic is enabled by the robot's interaction with surrounding objects through both suction and extrusion actuation. In this example, the robot first attaches to a user's item via suction and moves along with it (Figure 5f1-2), then pushes and releases the item through extrusion, allowing the user to retrieve it (Figure 5f3-4). This sequence portrays a playful and curious interaction pattern, mimicking a mischievous characteristic.

5.3 Multimodal wearables

In this section, to demonstrate the application of MorphingSkin in multimodal wearables, we present an interactive wrist brace that integrates both haptic and visual feedback.

Haptic feedback: We design two groups of extrusion actuators on the MorphingSkin, positioned on both the palmar and dorsal sides of the hand, respectively, with each group consisting of three actuators that deliver extrusion actuation (Figure 6a-b). When activated, these actuators create localized pressing sensations (described as "massaging feelings" by the volunteers during the test) on the skin (Figure 6c). All six actuators can be independently controlled to render spatio-temporal haptic feedback animations.

Visual feedback: We implemented two reflective displays located on both the inner and outer sides of the wrist (Figure 6a-b). The inner wrist features a red and continuous linear display bar that can represent continuously changing data, such as heart rate intensity or other physiological signals (Figure 6e). The outer wrist features a patterned blue display bar designed to convey more complex information, such as counters or timers (Figure 6d). Compared to light-emitting displays such as LED screens, these reflective displays serve as ambient displays that might provide more subtle, non-intrusive visual feedback, appearing to blend seamlessly into the human skin.

In addition, to demonstrate the compatibility of our MorphingSkin with existing electronics, we also integrated input and sensing modules into the wrist brace, including a heart rate sensor on the inner side of the wrist (Figure 6f1) and two touch buttons on the outer side of the wrist (Figure 6f2).

By collectively using both the multimodal actuators and the integrated sensors, the MorphingSkin wrist brace can support a variety of application scenarios. Combined with the portable driving hardware introduced in Section 6.2, further untethered operation is supported. We envision three scenarios using the MorphingSkin wrist brace. For example, during yoga practice, the wrist brace can deliver sequential pressing feedback on either side of the hand to indicate the intended movement direction (Figure 6g). In scenarios such as meditation, the wrist brace can perform synchronized, gentle pressing and releasing actions across all actuators, which may help users regulate their breathing rhythm (Figure 6h). In both cases, users can occasionally glance at the two reflective displays to gather useful information, such as checking the exercise session progress via the outer display, or understanding the heart rate intensity through the inner display. In a different scenario such

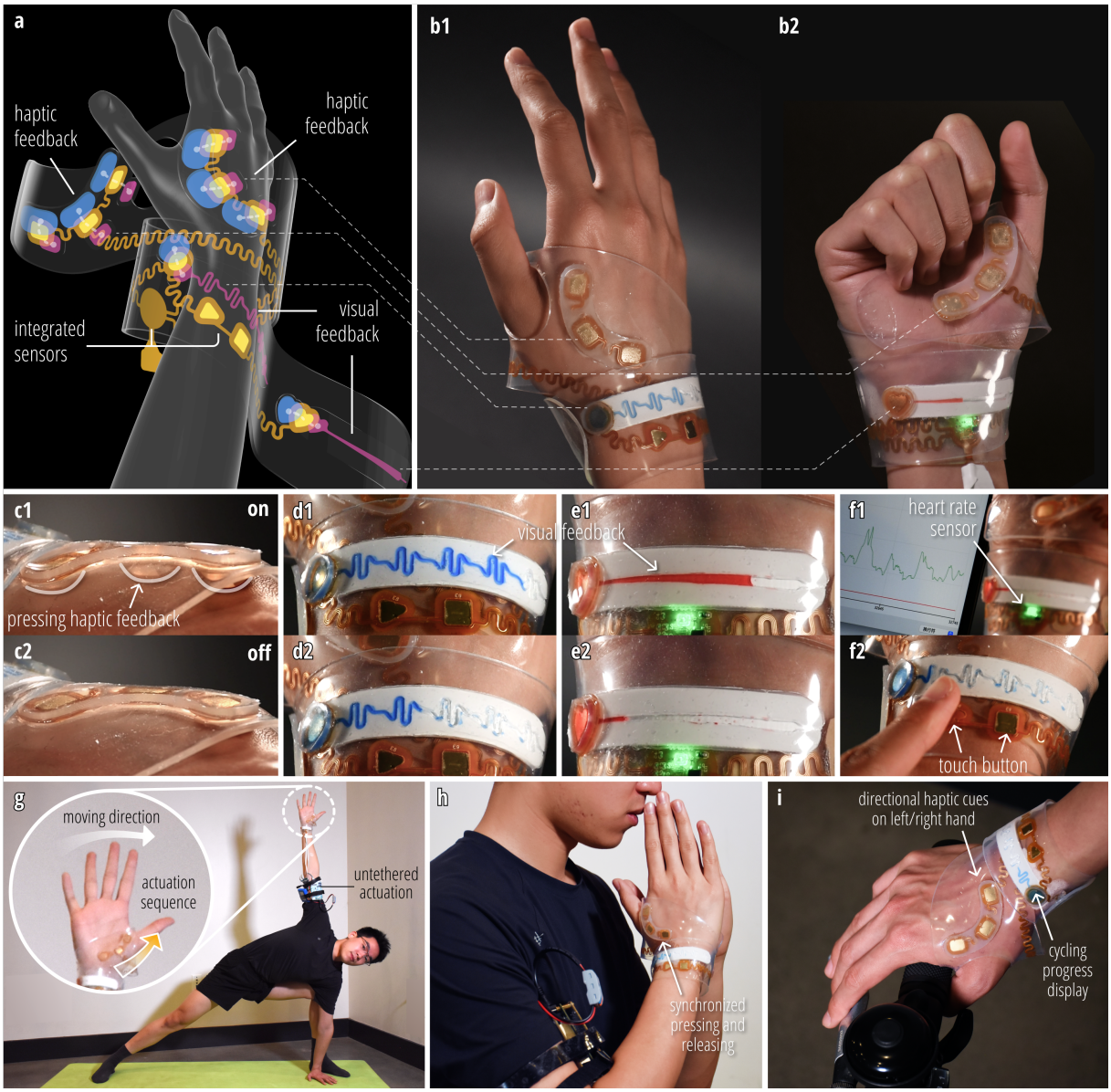

Figure 6: Application of MorphingSkin in multimodal wearables. (a) An interactive wrist brace is designed using MorphingSkin, containing both haptic and visual feedback and integrated sensors. (b) Photographs of the wrist brace in the worn state. (c) Haptic feedback by multiple extrusion actuators for spatio-temporal haptic animations. (d) Visual feedback by a reflection actuator in a patterned-bar shape. (e) Visual feedback by a reflection actuation in a linear-bar shape. (f) Integrated sensors, including a heart rate sensor and two touch buttons. We envision the usage of the MorphingSkin wrist brace in three scenarios, including (g) yoga practice, (h) meditation, and (i) outdoor cycling.

as outdoor cycling, when worn on both hands, the wrist braces can provide directional haptic cues, such as activating the haptic actuators on the left or right wrist brace to signal a left or right turn, and meanwhile present the cycling progress via the reflective display on the outer side of the wrist (Figure 6i).

5.4 Multimodal tangible display

In this section, to demonstrate the application of MorphingSkin for multimodal tangible displays, we present an interactive educational book featuring multiple dynamic effects, including refractive and reflective visual animations as well as shape movement. As illustrated in Figure 7a-b, we use MorphingSkin to develop a "magic

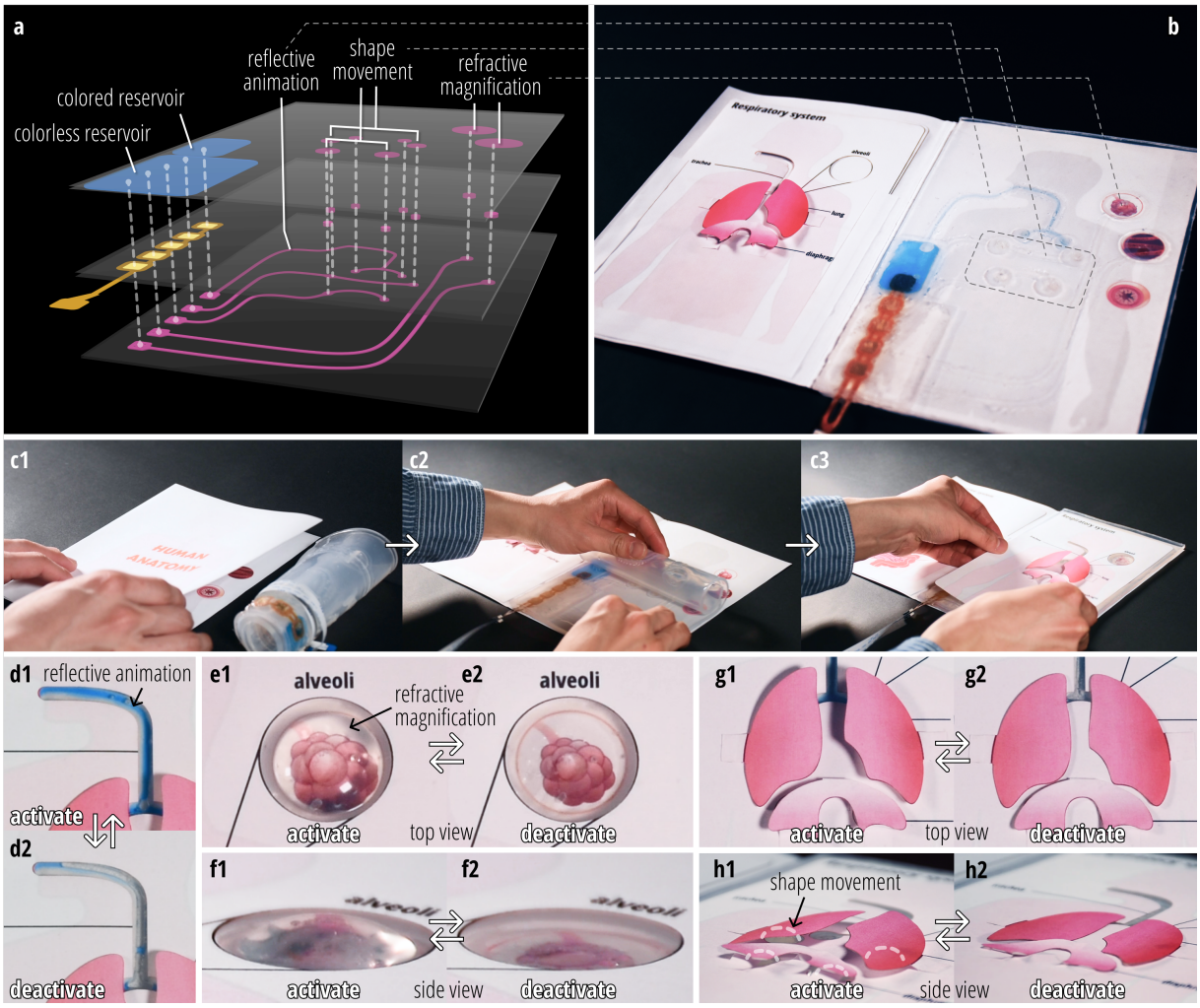

Figure 7: Application of MorphingSkin in multimodal tangible display. (a) A "magic page" using MorphingSkin is designed for a human anatomy book, providing dynamic effects, including reflective animation, refractive magnification, and shape movement. (b) Photograph of the "magic page" placed on the anatomy book with a respiratory-system theme card. (c) Usage process of the "magic page" that leverages flexibility for foldable storage. (d) Reflective animation that illustrates the airflow through the trachea. (e-f) Refractive magnification that mimics the volume changes of the alveoli. (g-h) Shape movement that represents the movement of the lungs and diaphragm.

page" within a human anatomy book, which illustrates the biological functional processes of different respiratory organs. As shown in Figure 7c, to use the magic page, the user unrolls the flexible magic page, places it on a background page, and then overlays it with a themed card representing the respiratory system.

Reflective animation Based on the reflection actuation, reflective visual animation is used to illustrate the airflow through the trachea. When activated, the actuator pumps the blue-colored working fluid from its reservoir into the trachea-shaped fluidic channel, simulating the inhalation phase (Figure 7d1). Upon deactivation, the fluid is withdrawn back into the reservoir, simulating the exhalation phase (Figure 7d2).

Refractive magnification Based on the refraction actuation, a visual magnification effect is utilized to mimic the volume changes of the alveoli during respiration. When activated, the working fluid inflates the output layer, causing it to expand and create a magnifying refractive effect, simulating the alveoli expansion during inhalation (Figure 7e1, f1). Upon deactivation, the output layer deflates and the refractive effect is reset, simulating alveolar recoil during exhalation (Figure 7e2, f2).

Shape movement Based on the kinematic motion actuation, shape movement is designed to represent the movement of the lungs and diaphragm. Upon activation, the inflating output layer pushes up the overlaid paper element, mimicking lung expansion and diaphragm contraction during inhalation (Figure 7g1, h1). When

deactivated, the output layer retracts, allowing the paper element to recover its original position, simulating lung deflation and diaphragm relaxation during exhalation (Figure 7g2, h2).

Notably, these actuators can be synchronously controlled to activate and deactivate, illustrating how multiple organs work in coordination within the respiratory system.

5.5 Dynamic lampshade

In this section, we demonstrate the application of MorphingSkin as a dynamic lampshade based on its multimodal actuation, including shape and optical changes, and their interaction with light.

As shown in Figure 8a-b, we design a lampshade wrapped around a non-diffusive light source using MorphingSkin, which contains a group of vertically oriented, strip-shaped shape-changing actuators functioning as dynamic soft lenses. Upon activation, the embedded EOPs pump working fluid from the backside reservoirs into these lenses, causing them to inflate and deform into a convex shape (Figure 8b2).

Figure 8c illustrates the dynamic light patterns projected onto the ground directly caused by the refraction of the light through the inflated lenses. When the lenses are inflated to a certain thickness, they focus the light onto the ground, forming concentrated light patterns in different directions.

Figure 8d shows another light effect, where the light patterns are projected onto a surrounding translucent diffuser film. Notably, due to gravity, the inflation of these soft lenses occurs progressively from bottom to top, thus dynamically refracting the light to produce a group of linear light patterns with variable lengths. The combination of multiple linear light patterns collectively provides an affordance for ambient visual display or aesthetic expression.

Figure 8e further demonstrates the usage of the shape-changing lampshade to actuate the texture changes on an overlaid kirigami surface. As the lenses inflate, the auxetic patterns on the kirigami surface selectively open at different locations, thereby altering the transmission behavior of light and creating a spatially varied illumination environment.

6 Fabrication and Implementation

6.1 Fabrication of MorphingSkin

Below, we detail the fabrication process for MorphingSkin devices with customized designs and both flexible and partially stretchable form factors. The fabrication process consists of four main steps: (1) Assemble the flexible EOP circuit, (2) coat the EOP layer, (3) fabricate and bond the elastic shells, and (4) install the working fluid.

6.1.1 Assemble the flexible EOP circuit. In this work, we employ industrial flexible printed circuits (FPCs) as the substrate electrodes to fabricate the EOP, which ensures both flexibility and partial stretchability compared to previous work [53, 55].

The electrode design for the EOPs is illustrated in Figure 9a. Each electrode features a central electrode mesh composed of a double-sided metal-covered surface. Within this mesh region, vias are arranged in a hexagonal pattern, with each via measuring 0.16 mm in diameter and spaced 0.37 mm apart, yielding an open area of approximately 17%. Surrounding the electrode mesh is a bonding region, where a minimum width of 2 mm is recommended to ensure adequate bonding and sealing quality. Although these EOP electrodes exhibit moderate flexibility (comparable to a thin copper sheet), we employ linear or serpentine traces with a narrow width to connect these EOP electrodes, which contributes the primary flexibility and partial stretchability to the overall circuit. Most of the electrodes are fabricated using double-sided FPCs, with a wire width of 0.25 mm and a spacing of 0.25 mm between adjacent traces or edges. The electrode surface is insulated and protected by polyimide soldermask except for the electrode mesh region. A detailed cross-sectional illustration is shown in Figure 9e, where the total thickness of a single layer of the electrode is approximately 0.11 mm. We fabricate the FPC electrodes from JLCPCB by uploading manually designed files.

A complete EOP unit consists of two electrodes that sandwich a pumping membrane and an adhesive layer. The pumping membrane is designed with a contour that extends 0.2 mm outward from the electrode mesh region, and fabricated using a Universal CO_2 laser cutting machine and Grade F borosilicate glass fiber filter paper as the material. To facilitate the assembly of multiple EOP units using flexible circuits, we introduce an approach using thermoplastic polyurethane (TPU) gaskets and heat pressing to bond the electrodes. The TPU gasket is designed to fill the gap between the pump membrane and the surrounding electrode region, with a thickness of approximately 0.4 mm, which is similar to the thickness of the pump membrane before applying the heat press. The gaskets are then 3D printed using NinjaFlex 85A water-translucent TPU filament on an Ultimaker 5 printer. Figure 9b shows the assembly process, where we first place one EOP electrode at the bottom, use tweezers to carefully place the pump membrane and TPU gasket in position, and place the second electrode on top. Carrier films are used on both the bottom and top to sandwich these components and maintain their position for the subsequent heat pressing process. We then apply the heat press to the components at 180°C for about 5 minutes, during which the TPU gaskets are expected to melt and as fully as possible fill the bonding region, ensuring a secure seal.

A sample of assembled EOPs with cured TPU adhesive is shown in Figure 9c. The total thickness of each EOP after heat pressing is about 0.4 mm, with a cross-sectional photograph shown in Figure 9d. Necessary electronic components, such as cable connectors, are then soldered onto the EOP circuit after the heat press. For certain FPC designs where heat pressing is impractical (e.g., due to pre-mounted electronic components), we follow prior work [53] and use laser-cut 3M 467MP double-sided adhesive tape as the bonding material.

6.1.2 Coat the EOP layer. Following the electrode assembly, we encapsulate the bonded EOP circuit with a layer of stretchable material that provides support for the MorphingSkin and separates the elastic shells located on both sides.

One option we have adopted for most prototypes in this project is using silicone as the coating material. Here, we use Smooth-On Sorta-Clear 12 as the coating material. The process involves first casting a bottom silicone layer, followed by placing and gluing the EOP circuit onto this layer, and then casting the top silicone layer. To facilitate accurate placement and alignment, a transparent glass

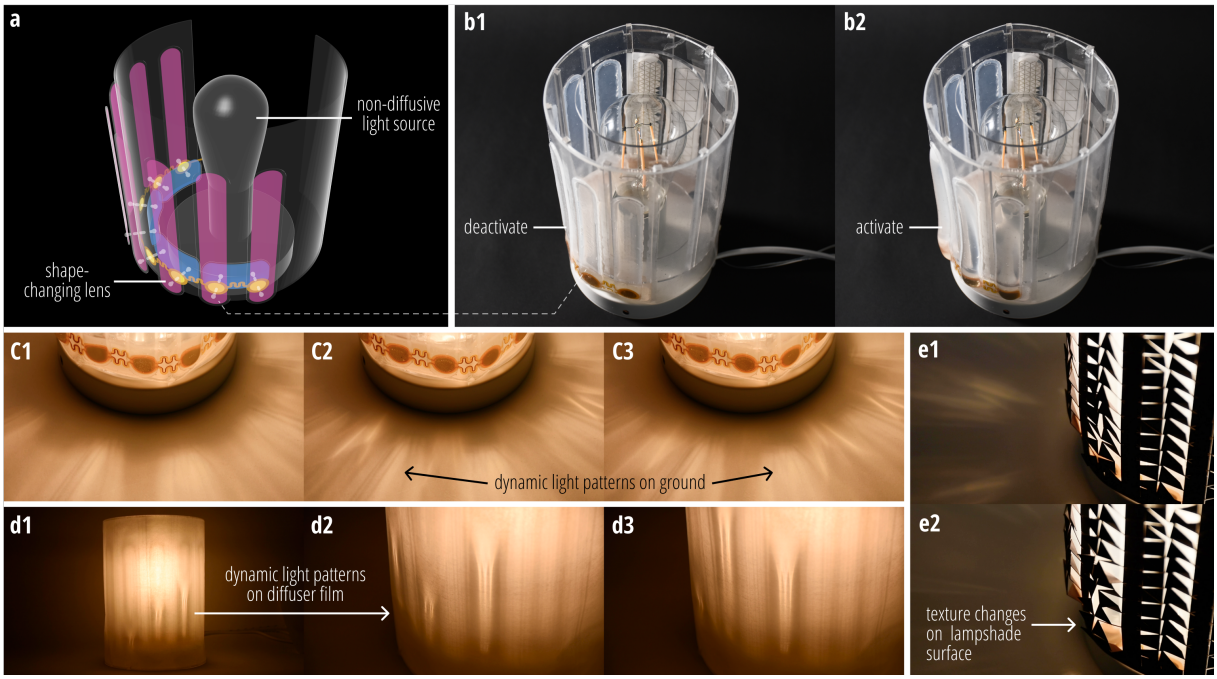

Figure 8: Application of MorphingSkin as a dynamic lampshade. (a) A lampshade using MorphingSkin is wrapped around a light source, containing a group of strip-shaped shape-changing actuators, which (b) deform into a convex shape when inflated, functioning as dynamic soft lenses. (c) Dynamic light patterns projected onto the ground in different directions caused by direct refraction. (d) Dynamic light patterns projected onto a diffuser film, displaying multiple linear patterns with variable lengths. (e) Texture changes on an overlaid kirigami surface that alters the illumination environment spatially.

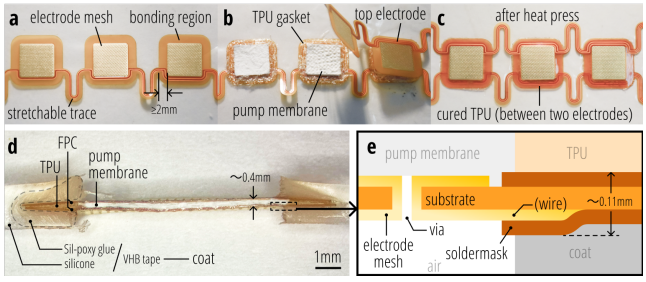

Figure 9: (a-c) Assembling the flexible EOP circuit. (d) Cross-section photography of the coated EOP layer. (e) Cross-section illustration of a single layer of EOP electrode.

plate is used as the base, with a printed sketch placed underneath. To keep the electrode mesh on the EOP circuit exposed and not blocked by silicone, we reserve hollow regions in the bottom silicone layer using mask tape (Figure 10a), and similarly protect the electrode mesh region on both sides of the EOP circuit with mask tape before casting the top silicone layer (Figure 10c). To ensure strong bonding and sealing between the EOP circuit surface and the silicone material, we apply Smooth-On Sil-Poxy glue to the contact surface, either on the silicone surface before placing the EOP circuit (Figure 10b), or on the electrode's bonding region after the circuit is in place (Figure 10c). To ensure that the EOP circuit is as vertically centered as possible within the encapsulation, we carefully design the thicknesses of the top and bottom silicone layers, along with all mask tapes used, shown in Figure 10a,c,d. The masks are constructed by stacking multiple layers of 0.1 mm-thick single-layer mask tape and laser cutting into custom shapes. The total coating thickness is around 1.2 mm to 1.5 mm. Once the top layer of silicone is fully cured, we carefully remove the mask tapes from both sides of the EOP circuit using tweezers. The fully encapsulated EOP circuit is shown in Figure 10e-f, with its cross-section displayed in Figure 9d.

We also proposed an alternative method that uses VHB tape as the coating material. While our observations suggest that the VHB tape may undergo debonding after several days, possibly degraded by the working fluid, this approach remains simple and fast to implement, making it a potential option for rapid testing. To fabricate the coating layer, we stack a bottom VHB layer, the EOP circuit, and a top VHB layer sequentially and then apply vertical pressure to increase the bonding and sealing quality (Figure 10g). We use 3M VHB 4905 tape with a thickness of 0.5 mm as both the bottom and the top VHB layer. The total coating thickness is around 1.0 mm to 1.3 mm. Both VHB layers are pre-cut using a Universal laser cutting machine to create the hollow regions that expose the electrode mesh region on the EOP circuit. To facilitate handling, transfer films are used to hold, transfer, and apply the VHB tapes. The final VHB-coated EOP circuit is shown in Figure 10h-i.

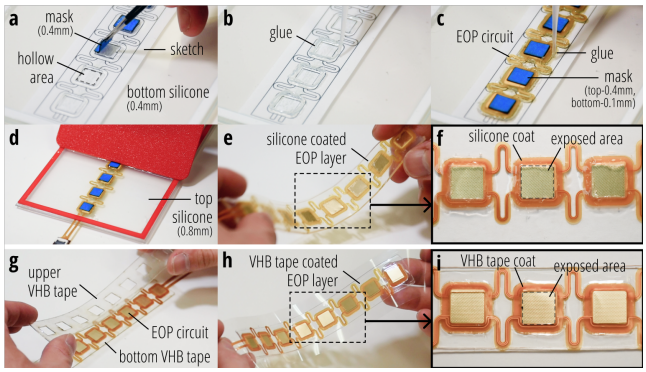

Figure 10: Coating the EOP layer with (a-f) silicone material and (g-i) VHB tape.

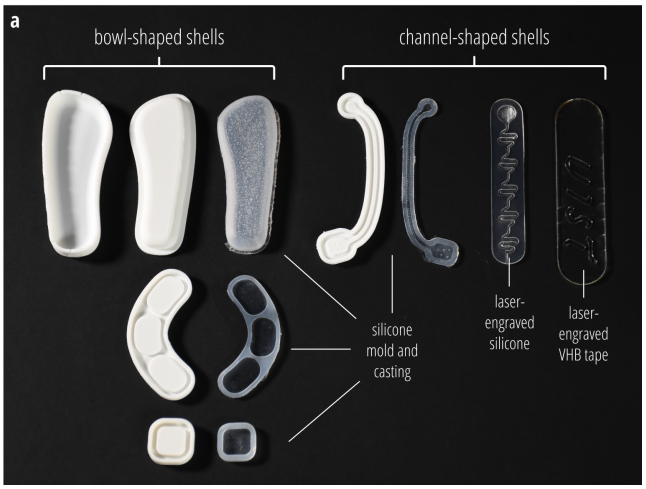

Figure 11: Design and fabrication of the elastic shells.

6.1.3 Fabricate and bond the elastic shells. Next, we fabricate elastic shells that are bonded to both sides of the MorphingSkin. These shells serve various functions, including output layers, connection layers, or reservoir layers.

Depending on the geometric configuration of the shell, we introduce two fabrication methods: The first type is a bowl-shaped shell, which features a central cavity with a certain depth to accommodate liquid, surrounded by a continuous rim of uniform height that serves as the bonding surface to the coating layer, as shown in Figure 11. These shells are used mainly as shape-changing output layers or as liquid reservoirs. In this work, we fabricate these bowl-shaped shells by casting silicone into 3D-printed molds. The second type is channel-shaped shells, which consist of relatively shallow (e.g., 0.5mm deep) but more complex two-dimensional fluidic channels, similarly surrounded by a uniform height bonding surface, shown in Figure 11. These shells are typically used as connection layers or, in some cases (e.g., reflective displays), as output layers. To fabricate these channel-shaped shells, we either cast silicone using 3D-printed molds, or engrave the channels directly into the surface of silicone or VHB tape using a Universal laser cutting machine, following previous work [42]. Depending on the fabrication method, the desired softness, and the optical clarity, we select Smooth-On Ecoflex 00-30, SORTA-Clear 12, or 3M VHB 4905 tape as the shell materials.

Once the shells are fabricated, they are bonded to the coating layer using different techniques, depending on the materials and the shell geometry. When both the shells and the coating layer are made of VHB tape, the shells are carefully aligned and pressed onto the coating layer using a transfer film. When the bonding surfaces involve VHB tape and silicone, or both are silicone, we use Smooth-On Sil-Poxy glue as the bonding adhesive. For shells with large bonding areas, the glue is applied uniformly using a 3D printed stencil (Figure 12a1). For shells with narrow bonding rims, the glue is manually dispensed onto the shell's bonding surfaces using a syringe (Figure 12a2). After the glue is applied, the shells are aligned and pressed onto the coating layer using a transfer film (Figure 12b).

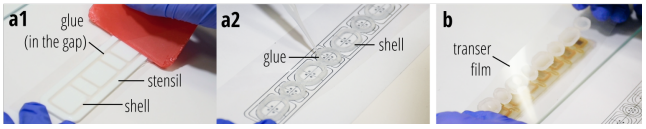

Figure 12: Bonding of the elastic shells.

6.1.4 Install the working fluid. After the shells are assembled and bonded, we install the working fluid into the MorphingSkin. Following previous work [55], we use a syringe with a 30G needle to first evacuate the air inside each actuator and then inject the working fluid (Figure 13a). This process is repeated as necessary until the internal air is fully displaced and replaced by the working fluid. The silicone used to construct the device exhibits self-sealing behavior upon removal of the 30G needle. When required, we use Smooth-On Sil-Poxy glue to seal any leakage points. In this work, we use Propylene Carbonate as the working fluid. To achieve dynamic display in reflective modality, we color the working fluid with alcohol-based ink.

A fully assembled MorphingSkin device after fluid installation is shown in Figure 13b, which is capable of undergoing multiple types of deformation, including bending, twisting, and stretching, shown in 13c.

6.2 Driving hardware system

In this work, for rapid testing in most of the demonstrations, we adopted a similar driving hardware as previous work [70], which consists of a high-voltage DC converter and a series of relays manually controlled via an Arduino board. Unless otherwise specified, all actuations throughout the paper were conducted at ±250 V.

Moreover, to support demonstrations requiring more complex programmed actuations and untethered control, we developed a portable version of the driving hardware system, as introduced below. As shown in Figure 14a, the hardware system is built around a Raspberry Pi Zero 2 W microcontroller, a DC-DC boost converter

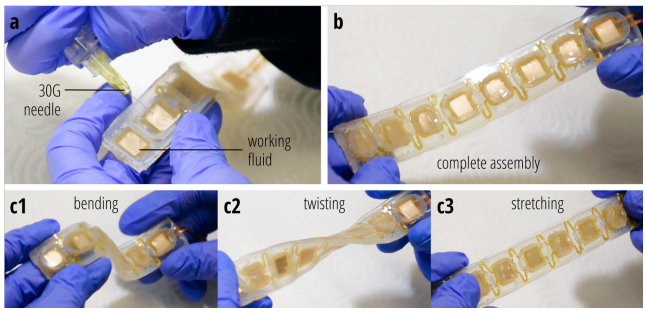

Figure 13: (a-b) Installing the working fluid and finishing. (c) The fully assembled MorphingSkin device undergoing multiple types of deformation.

(HRB12150-250DG-20W), and four 8-channel serial-to-parallel converters with high-voltage push-pull outputs (HV513). The DC-DC boost converter steps up a low input voltage (e.g., 12 V) to a high output voltage (e.g., 150–250 V), where the output voltage can be pre-configured by adjusting a control knob on the converter module. The HV513 serial-to-parallel converters are used to assign high-voltage signals to designated output ports. The total maximum output power of all ports is 20 W. The hardware is connected to the EOP circuits via a 0.5 mm pitch flat flexible cable (FFC). The power of the hard hardware system is supplied by 12 V lithium batteries or chargers.

The four 8-channel serial-to-parallel converters provide a total of 32 output channels, which comprise 16 ports, with each port using a pair of channels. We can program each port with Python to output positive voltage, negative voltage, or zero voltage in time sequence, thus using each port to independently control a single EOP actuator in the MorphingSKin device.

Figure 14b shows the size of the hardware system in non-tethered usage, with a volume of approximately 10x6x2 cm. The portability enables the usage of MorphingSkin in mobile applications such as wearable devices.

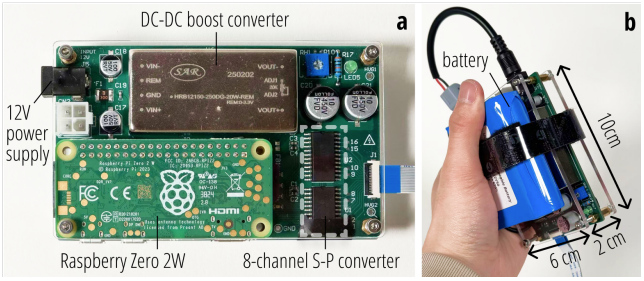

Figure 14: Driving hardware system that contains 16 programmable output ports with pre-set output voltages ranging from 150 V to 250 V, enabling untethered operation of MorphingSkin devices.

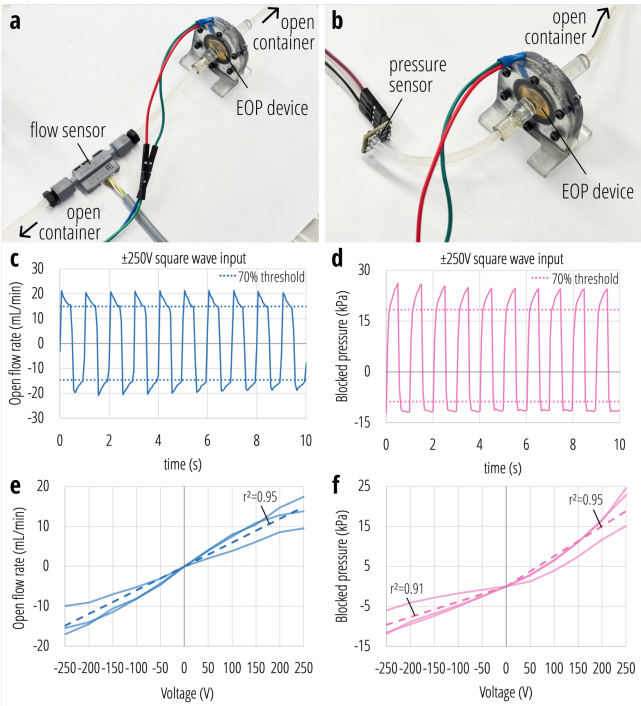

Figure 15: Technical evaluation of the open flow rate and the blocked pressure of the EOP device.

7 Technical Evaluation

7.1 Open flow rate and blocked pressure

In this experiment, we evaluated the performance of the EOP that follows the fabrication process in this work, including the open flow rate and blocked pressure.

The experiment setup is shown in Figure 15a A 12mm-diameter, round-shaped EOP is fixed in a specially designed flow cell, with its two sides sealed off from each other to allow the working fluid to flow through the EOP. When measuring the flow rate, a calibrated SLF3S-0600F Liquid Flow Sensor was connected in series with the EOP flow cell, and the two ends of the device were extended below the liquid surface of an open container filled with working fluid through silicone tubes, as shown in Figure 15a. When measuring pressure, we removed the flow sensor and connected the MS5837-30BA pressure sensor on the same side in a blocked manner, with the other end staying the same, as shown in Figure 15b.

We injected the working fluid into the entire device using a syringe and evacuated the internal air bubbles. As in prior work [55], we used a 1 Hz square wave signal to drive the test EOP device. The amplitude of the square wave was set at each level from 0 V to 250 V in increments of 50 V, with each test lasting at least 10 seconds. We used an adjustable DC high-voltage boost converter, powered by a 12 V power supply, to generate the driving voltage between 0V to 250 V, and used two relays controlled by an Arduino Nano board to produce the desired square-wave voltage signal applied to the test device. Each experiment was repeated three times using different EOP devices.

7.1.1 Data collection and analysis. We used the software on the PC to collect the data from the flow sensor, and used the controlled Arduino Nano to collect the data from the pressure sensor. After obtaining the data, for each voltage level U, we computed the average of the test data points that exceed 70% of the maximum (for the positive half-cycle) or minimum (for the negative half-cycle) value separately, which then served as the performance metric under $+U$ and $-U$, respectively. In total, we obtained the open flow rate and blocked pressure performance at 10 voltage levels ranging from -250 V to +250 V, in 50 V increments, excluding 0 V.

7.1.2 Results. Figure 15c-d show the open flow rate and the blocked pressure data under 10 typical cycles within a test under 250 V voltage level. We observed a maximum instantaneous flow rate of approximately 20 mL/min on the EOP in our test with an area of 113 mm^2, and a maximum instantaneous pressure of approximately 25 kPa, which are at the same order of magnitude as the previous work [48] and [55], respectively. These results indicate that the EOP produced by the fabrication process in this paper might have performance comparable to the previous work.

Figure 15e shows the relationship between the open flow rate and the applied voltage in three tests, where all three tests showed a consistent linear relationship, similar to the previous work [55]. However, one group of the data showed an overall weak response, and we inferred that this might be due to the manual assembly error of the test EOP. The dashed line in the figure shows the result of linear fitting for all three groups of data, with $r^2 = 0.95$ and a slope of 59.6 μL/min/V.

Figure 15f presents the relationship between the blocked pressure and the applied voltage on three tests. Among them, one set of the data showed a relatively weak overall response, which we similarly attributed to manual assembly error. Notably, across all three test sets, we observed a consistent asymmetric response regarding the blocked pressure, where either the positive or negative half-cycle exhibited slightly stronger performance. To normalize this asymmetry for comparison, we plot the data with the stronger overall response in the positive voltage range, and the weaker one in the negative range. As a result, all three test sets demonstrated a similar trend in their response patterns. We assumed that this asymmetric response might be attributed to the asymmetric property of the materials in EOP (e.g., the filter paper) or the asymmetric assembling operation during the fabrication process. Accordingly, we performed linear fitting on the data of positive voltage and negative voltage separately, with r^2 values of 0.95 and 0.91, and slopes of 75.4 Pa/V and 38.4 Pa/V, respectively.

7.2 Power consumption, heat generation, and durability

In this experiment, we evaluated several long-term engineering performance metrics of the MorphingSkin actuator, including power consumption, heat generation, and durability, based on a typical and simple MorphingSkin test device.

The experimental setup is illustrated in Figure 16a. The MorphingSkin device, made into a shape-changing actuator, is horizontally mounted at the center of the setup. The actuator is based on a 12 mm-diameter round-shaped EOP, with an output layer and a reservoir layer made from Smooth-On Ecoflex 00-30 silicone, directly attached to either side. Approximately 0.53 mL of working fluid is injected into the actuator to fully occupy the internal volume. A square wave signal with a 6-second period and 100 V amplitude was used to drive the actuator. During each cycle, at the first 3-second inflation phase, we applied +100 V to the device, causing the EOP to pump the entire working fluid from the reservoir to the output layer, resulting in an extrusion deformation (Figure 16b1-4); the subsequent 3-second deflation phase applies -100 V, pumping the fluid back into the reservoir, reversing the deformation (Figure 16b4-6). We used the same hardware system as Section 7.1 to provide the driving voltage signals. The experiment ran continuously for 1 hour, totaling 600 actuation cycles.

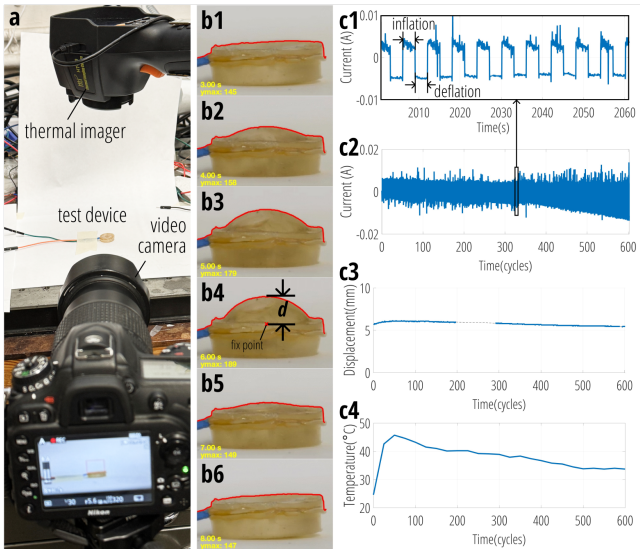

Figure 16: Technical evaluation of the power consumption, heat generation, and durability of a typical and simple MorphingSkin test device.

7.2.1 Data collection and analysis. We used a side-view camera capturing video at 25 fps to record the deformation behavior of the actuator, and then used a MATLAB-based computer vision program to extract the upper contour of the device and compute the peak displacement in each cycle. The peak displacement is defined as the vertical distance between the actuator's highest point and the fixed base plane height in each cycle (Figure 16b4). We used a top-view thermal camera that captures video at 25 fps to record the temperature of the device. We manually extracted the maximum temperature of the device every 25 cycles from the captured video. We used a 1-ohm sampling resistor in series with the circuit to measure the voltage across it at a 100 Hz sampling rate using a NI-6341 DAQ. The device's current was then calculated using Ohm's law. To reduce noise from the measurement equipment, we removed the outliers that are larger than 50 mA, and used a 6-order Butterworth low-pass filter to smooth the noise.

7.2.2 Results. Figure 16c1 shows the current over a 60-second window. We observed an average current of 2.43 mA during the

inflation phase and 4.33 mA during the deflation phase. The asymmetry in current magnitude and waveform between the two phases may be attributed to differences in pressure resistance encountered by the EOP, when transferring the working fluid to deform versus restore the output shell. The average power consumption across the 10 cycles is 0.36 W.

Figure 16c2 shows the current over all cycles, where the current range remained stable throughout, except for a gradual increase in the deflation-phase current after about 350 cycles. We hypothesize this may result from drift in the sampling resistor's resistance or a cumulative static offset in the measurement device.

Figure 16c3 presents the peak displacement over all cycles. The average displacement is 6.0 mm, with a standard deviation of 0.080 mm. Note that the dashed segment illustrates the region where the camera loses focus. We observed a slight initial increase in displacement followed by a gradual decline starting around cycle 50. We infer that this may be caused by gas generation from impurities in the working fluid during operation, where the gas accumulation in the output layer increased the internal volume, leading to a rise in peak displacement, and the gas buildup in the reservoir blocked the pumping area of the EOP, reducing the pumping amount of the working fluid and consequently decreasing the peak displacement.

Figure 16c4 shows the temperature evolution during the test. The maximum surface temperature rose from 25°C to 46°C in the first 5 minutes, then gradually decreased to around 35°C over the remaining time. We attribute this decline to the accumulation of air bubbles in the reservoir, which may block the effective pumping area of the EOP, reducing both the fluid transfer amount and the accompanying heat generation.

7.3 Stretchability and Failure test

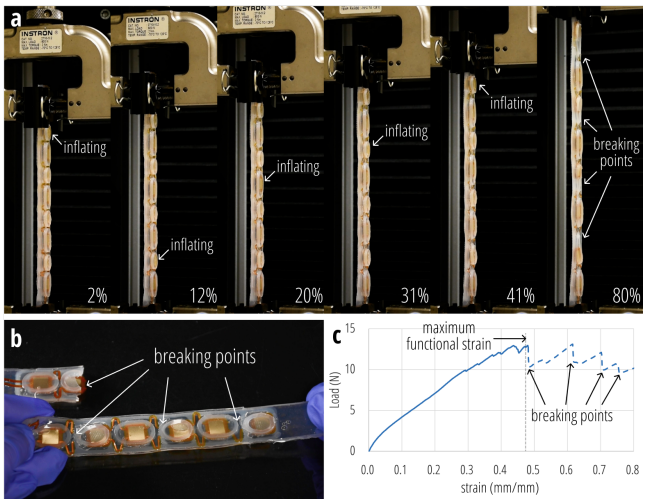

Figure 17: Technical evaluation of the stretchability and the failure test of a typical MorphingSkin test device.

In this experiment, we tested the maximum tensile strain by a tensile test and observed the failure mode, based on a typical MorphingSkin test device.

The test device is designed with eight actuators arranged in a row, where each actuator contains an EOP with an 8 by 8mm square shape, spaced 17mm apart, and connected using stretchable serpentine traces, following the same design shown in Figure 9a. During the fabrication process, we coated the EOP circuit with 1.5mm-thick Smooth-on Sorta-Clear 12, and then attached reservoirs and output layers made of Smooth-on Ecoflex 0030 on either side of the coated EOP layer, forming the complete actuators that are capable of extrusion-style shape changes. The final assembled test device is the same as that shown in Figure 13b, except that we added a 3 cm-long solid silicone on both ends of the test device for attaching to the fixtures of the tensile machine. During the test, we stretched the test device vertically at a rate of 145 mm/min, starting from 0% strain. Simultaneously, we activated the eight actuators on the test device in sequence, under a 100 V input and a 1-second duration, to continuously observe the working state of the device until it failed. We used a video camera to record the stretching process and collected the load-strain curve from the test software.

7.3.1 Results. Figure 17a,c show the stretching process and the load-strain curve from the stretching test. We observed that the test device exhibited approximately linear elastic deformation before about 47% strain and remained functional in the video. After that, a break occurred in the EOP circuit, causing part of the actuators to fail. In total, four circuit breaks occurred successively as the device was stretched to 80% strain. Figure 17b shows the photo of the test device after the tensile test, where we observed that all four break points on the EOP circuit occurred at the connection points between the serpentine trace and the EOP area, and the actuators near the break points all experienced leakage, possibly caused by the accompanying cracks or breaks of the silicone coating. The actuators without circuit breaks, however, did not exhibit leakage. From the above, we infer that the factor limiting the maximum tensile strain of this test case might be the maximum tensile strain of the EOP circuit. That is to say, in future work, the overall stretchability of MorphingSkin could potentially be improved by optimizing the design of the serpentine traces or adopting fully stretchable circuits, while remaining within the tensile limits of other materials (e.g., silicone) and the bonding methods used in the device.

8 Limitation and Future Work

8.1 Material and fabrication technique

Although MorphingSkin in our work has achieved progress in flexibility and stretchability compared to previous EOP actuators, enabled by the introduction of new materials and fabrication processes, several limitations still remain.

For example, during operation, we continue to observe that propylene carbonate gradually generates gas, and the colored alcohol-based ink dissolved in the propylene carbonate slowly fades. These phenomena may reduce the actuator's overall performance over time. Additionally, the VHB tape tends to debond within 48 hours as in contact with propylene carbonate, leading to leakage issues of the actuator. Manual fabrication errors, such as misalignment or poor sealing quality, can also negatively affect the actuator performance, such as weakening the pumping flow rate and pressure, or increasing the heat generation.

Future work could investigate the underlying mechanisms behind these material failures and adopt better material and digital fabrication strategies to enhance the durability, stability, and consistency of the MorphingSkin devices.

8.2 Technical research of MorphingSkin

In this work, we demonstrated the multimodal actuation by MorphingSkin on a flexible platform. Nevertheless, to introduce the MorphingSkin actuators to broader engineering and design contexts, several avenues for future work remain.

One direction involves investigation of the effect of mechanical strain, particularly stretching, on the actuator's performance. In the current implementation, stretching in MorphingSkin primarily occurs in the serpentine interconnects of the flexible printed circuits and the surrounding elastic shell. The EOPs embedded within the non-stretchable regions of the FPCs experience only bending and are not designed to stretch. This structural constraint may help mitigate the impact of overall device strain on the EOP's performance. However, the exact impact of mechanical deformation (e.g., bending, squeezing) on the FPC-based EOPs still requires further experimental investigation.

Other directions involve studies of the relationships between detailed design parameters (e.g., EOP design [6], output shell geometry, and material stiffness) and the resulting multimodal actuation performance. Standardized actuator designs based on MorphingSkin could be established to serve as a benchmark for future research. Additionally, the integration of sensing and precise control of the MorphingSkin actuators still remains crucial to enhance the controllability and the programmability of the multimodal actuation capabilities.

8.3 User experience and feedback

In this work, we demonstrated a wide range of potential applications for MorphingSkin, showing both the breadth and engineering feasibility of how MorphingSkin integrates multimodal output modalities into a flexible, partially stretchable, self-contained, and even untethered interactive platform. However, the user experience and feedback have only been explored to a limited extent in this work.

We believe several directions would be worth investigating via future user studies or design workshops: (1) Haptic sensations: How do users perceive the haptic feedback of MorphingSkin when worn on the body? How are these sensations affected by design factors, such as actuator sizes, pressure levels, and body location? What cognitive information can be encoded via spatio-temporal haptic sequences provided by MorphingSkin? (2) Robotic skin: What other functional designs might users envision in daily life, given the robotic skins with unique outputs, such as positive/negative pressure or dynamic textures? Where might such skins be deployed, such as on existing robotic platforms or everyday objects? (3) Multimodal display: What other information or visual effects might users find expressible through combinations of reflection, refraction, and shape change? How do these modalities interact with each other?

While we acknowledge that a full investigation of these questions lies beyond the scope of this paper, we propose an initial approach to evaluating user experience or the higher-level actuation behaviors, by combining the technical evaluation results (i.e., blocked pressure and open flow rate) and established knowledge, such as analytical or simulation methods and also psychophysical studies. For example, by simply multiplying the blocked pressure by the actuator surface area, we can estimate the pressing force applied to human skin, and then predict the user's sensations by comparing it with the skin sensitivity on a certain body region [18]. We can also use Finite Element Analysis (FEA) to simulate the shape changes and speed of the elastic shells under hydraulic flow and the resulting changes in surface texture or light refraction path, and then predict user's emotional or cognitive perceptions during interaction by comparing with previous studies on expressive robotic textures [23] or illuminating materials [61]. These insights may also inform the future development of application-specific design and simulation tools.

9 Conclusion

In this work, we present MorphingSkin, a skin-like platform that integrates multimodal hydraulic actuation based on flexible EOPs. We introduce the structure composition of MorphingSkin and the versatile design space for multimodal actuation in force, shape, optical, and weight domains. We demonstrate a wide range of applications using MorphingSkin, including actuating surfaces on companion robots and gripper fingers, multimodal wearables, and physical interaction contexts such as dynamic lampshades and tangible displays. We detail the fabrication process for MorphingSkin devices, along with a portable driving hardware system that enables untethered operation. Lastly, we present three groups of technical evaluations of the MorphingSkin system, which show comparable hydraulic performance to prior work. Through this work, we envision the future of using MorphingSkin technology for interactive surfaces that integrate flexible form factors and multimodal actuation capabilities.

Acknowledgments

This work was supported by the First Year Fellowship from the Mechanical Engineering Department at UC Berkeley and the National Science Foundation 2427455 (CAREER). We thank Hajun Lee for the insights on the fabrication techniques and all the other lab members for brainstorming and discussion during the project.

References

[1] Lea Albaugh, Scott Hudson, and Lining Yao. 2019. Digital Fabrication of Soft Actuated Objects by Machine Knitting. In *Proceedings of the 2019 CHI Conference on Human Factors in Computing Systems (CHI '19)*. Association for Computing Machinery, New York, NY, USA, 1–13. doi:10.1145/3290605.3300414

[2] Kanon Aoyama, Takafumi Morita, Ziyuan Jiang, Yu Kuwajima, Tomoka Kurosawa, Naoki Hosoya, Shingo Maeda, and Yasuaki Kakehi. 2025. Liquebits: Colored Expressive Control of Liquid Fiber based on Electrohydrodynamics Actuation. In *Proceedings of the Nineteenth International Conference on Tangible, Embedded, and Embodied Interaction (TEI '25)*. Association for Computing Machinery, New York, NY, USA, 1–12. doi:10.1145/3689050.3704934

[3] Jas Brooks, Noor Amin, and Pedro Lopes. 2023. Taste Retargeting via Chemical Taste Modulators. In *Proceedings of the 36th Annual ACM Symposium on User Interface Software and Technology (UIST '23)*. Association for Computing Machinery, New York, NY, USA, 1–15. doi:10.1145/3586183.3606818

[4] Thomas J. K. Buchner, Toshihiko Fukushima, Amirhossein Kazemipour, Stephan-Daniel Gravert, Manon Prairie, Pascal Romanescu, Philip Arm, Yu Zhang, Xingrui Wang, Steven L. Zhang, Johannes Walter, Christoph Keplinger, and Robert K. Katzschmann. 2024. Electrohydraulic musculoskeletal robotic leg for agile, adaptive, yet energy-efficient locomotion. *Nature Communications* 15, 1 (Sept. 2024),

7634. doi:10.1038/s41467-024-51568-3 Publisher: Nature Publishing Group.

[5] Vito Cacucciolo, Jun Shintake, Yu Kuwajima, Shingo Maeda, Dario Floreano, and Herbert Shea. 2019. Stretchable pumps for soft machines. *Nature* 572, 7770 (Aug. 2019), 516–519. doi:10.1038/s41586-019-1479-6 Number: 7770 Publisher: Nature Publishing Group.

[6] Hsu-Feng Chang and Shyang-Jye Chang. 2025. Design optimization and performance enhancement of electroosmotic pumps for tactile applications using Taguchi-based methodology. *Sensors and Actuators A: Physical* 389 (Aug. 2025), 116568. doi:10.1016/j.sna.2025.116568

[7] Yanjun Chen, Xuewei Liang, Si Chen, Yuwen Chen, Hongnan Lin, Hechuan Zhang, Chutian Jiang, Feng Tian, Yu Zhang, Shanshan Yao, and Teng Han. 2022. HapTag: A Compact Actuator for Rendering Push-Button Tactility on Soft Surfaces. In *Proceedings of the 35th Annual ACM Symposium on User Interface Software and Technology (UIST '22)*. Association for Computing Machinery, New York, NY, USA, 1–11. doi:10.1145/3526113.3545644

[8] Tingyu Cheng, Jung Wook Park, Jiachen Li, Charles Ramey, Hongnan Lin, Gregory D. Abowd, Carolina Brum Medeiros, HyunJoo Oh, and Marcello Giordano. 2022. PITAS: Sensing and Actuating Embedded Robotic Sheet for Physical Information Communication. In *Proceedings of the 2022 CHI Conference on Human Factors in Computing Systems (CHI '22)*. Association for Computing Machinery, New York, NY, USA. doi:10.1145/3491102.3517532 event-place: New Orleans, LA, USA.

[9] Kyung Yun Choi, Jinmo Lee, Neska ElHaouij, Rosalind Picard, and Hiroshi Ishii. 2021. aSpire: Clippable, Mobile Pneumatic-Haptic Device for Breathing Rate Regulation via Personalizable Tactile Feedback. In *Extended Abstracts of the 2021 CHI Conference on Human Factors in Computing Systems (CHI EA '21)*. Association for Computing Machinery, New York, NY, USA, 1–8. doi:10.1145/3411763.3451602

[10] Alexandra Delazio, Ken Nakagaki, Roberta L. Klatzky, Scott E. Hudson, Jill Fain Lehman, and Alanson P. Sample. 2018. Force Jacket: Pneumatically-Actuated Jacket for Embodied Haptic Experiences. In *Proceedings of the 2018 CHI Conference on Human Factors in Computing Systems (CHI '18)*. Association for Computing Machinery, New York, NY, USA, 1–12. doi:10.1145/3173574.3173894

[11] Jialin Deng, Patrick Olivier, Josh Andres, Kirsten Ellis, Ryan Wee, and Florian Floyd Mueller. 2022. Logic Bonbon: Exploring Food as Computational Artifact. In *CHI Conference on Human Factors in Computing Systems*. ACM, New Orleans LA USA, 1–21. doi:10.1145/3491102.3501926

[12] Laura Devendorf, Joanne Lo, Noura Howell, Jung Lin Lee, Nan-Wei Gong, M. Emre Karagozler, Shiho Fukuhara, Ivan Poupyrev, Eric Paulos, and Kimiko Ryokai. 2016. "I Don't Want to Wear a Screen": Probing Perceptions of and Possibilities for Dynamic Displays on Clothing. In *Proceedings of the 2016 CHI Conference on Human Factors in Computing Systems (CHI '16)*. Association for Computing Machinery, New York, NY, USA, 6028–6039. doi:10.1145/2858036.2858192

[13] Amir Firouzeh, Ayana Mizutani, Jonas Groten, Martin Zirkl, and Herbert Shea. 2024. PopTouch: A Submillimeter Thick Dynamically Reconfigured Haptic Interface with Pressable Buttons. *Advanced Materials* 36, 8 (2024), 2307636. doi:10.1002/adma.202307636 _eprint: https://onlinelibrary.wiley.com/doi/pdf/10.1002/adma.202307636.

[14] Jack Forman, Ozgun Kilic Afsar, Sarah Nicita, Rosalie Hsin-Ju Lin, Liu Yang, Megan Hofmann, Akshay Kothakonda, Zachary Gordon, Cedric Honnet, Kristen Dorsey, Neil Gershenfeld, and Hiroshi Ishii. 2023. FibeRobo: Fabricating 4D Fiber Interfaces by Continuous Drawing of Temperature Tunable Liquid Crystal Elastomers. In *Proceedings of the 36th Annual ACM Symposium on User Interface Software and Technology (UIST '23)*. Association for Computing Machinery, New York, NY, USA, 1–17. doi:10.1145/3586183.3606732

[15] Jesse T. Gonzalez and Scott E. Hudson. 2022. Layer by Layer, Patterned Valves Enable Programmable Soft Surfaces. *Proc. ACM Interact. Mob. Wearable Ubiquitous Technol.* 6, 1 (March 2022), 12:1–12:25. doi:10.1145/3517251

[16] Daniel Groeger and Jürgen Steimle. 2018. ObjectSkin: Augmenting Everyday Objects with Hydroprinted Touch Sensors and Displays. *Proc. ACM Interact. Mob. Wearable Ubiquitous Technol.* 1, 4 (Jan. 2018), 134:1–134:23. doi:10.1145/3161165

[17] Sebastian Günther, Florian Müller, Dominik Schön, Omar Elmoghazy, Max Mühlhäuser, and Martin Schmitz. 2020. Therminator: Understanding the Interdependency of Visual and On-Body Thermal Feedback in Virtual Reality. In *Proceedings of the 2020 CHI Conference on Human Factors in Computing Systems*. ACM, Honolulu HI USA, 1–14. doi:10.1145/3313831.3376195

[18] Doyeon Han, Moonyoung Park, Junsuk Choi, Heonseop Shin, Donghwan Kim, and Sungsoo Rhim. 2022. Assessment of Pain Onset and Maximum Bearable Pain Thresholds in Physical Contact Situations. *Sensors (Basel, Switzerland)* 22, 8 (April 2022), 2996. doi:10.3390/s22082996

[19] Teng Han, Fraser Anderson, Pourang Irani, and Tovi Grossman. 2018. HydroRing: Supporting Mixed Reality Haptics Using Liquid Flow. In *Proceedings of the 31st Annual ACM Symposium on User Interface Software and Technology (UIST '18)*. Association for Computing Machinery, New York, NY, USA, 913–925. doi:10.1145/3242587.3242667 event-place: Berlin, Germany.

[20] Violet Yinuo Han, Abena Boadi-Agyemang, Yuyu Lin, David Lindlbauer, and Alexandra Ion. 2023. Parametric Haptics: Versatile Geometry-based Tactile Feedback Devices. In *Proceedings of the 36th Annual ACM Symposium on User Interface Software and Technology (UIST '23)*. Association for Computing Machinery, New York, NY, USA, 1–13. doi:10.1145/3586183.3606766

[21] Ollie Hanton, Zichao Shen, Mike Fraser, and Anne Roudaut. 2022. FabricatINK: Personal Fabrication of Bespoke Displays Using Electronic Ink from Upcycled E Readers. In *Proceedings of the 2022 CHI Conference on Human Factors in Computing Systems (CHI '22)*. Association for Computing Machinery, New York, NY, USA, 1–15. doi:10.1145/3491102.3501844

[22] Felix Heibeck, Basheer Tome, Clark Della Silva, and Hiroshi Ishii. 2015. uniMorph: Fabricating Thin Film Composites for Shape-Changing Interfaces. In *Proceedings of the 28th Annual ACM Symposium on User Interface Software & Technology*. ACM, Charlotte NC USA, 233–242. doi:10.1145/2807442.2807472

[23] Yuhan Hu and Guy Hoffman. 2023. What Can a Robot's Skin Be? Designing Texture-changing Skin for Human–Robot Social Interaction. *J. Hum.-Robot Interact.* 12, 2 (2023), 26:1–26:19. doi:10.1145/3532772

[24] Hiroshi Ishii, Daniel Leithinger, Sean Follmer, Amit Zoran, Philipp Schoessler, and Jared Counts. 2015. TRANSFORM: Embodiment of "Radical Atoms" at Milano Design Week. In *Proceedings of the 33rd Annual ACM Conference Extended Abstracts on Human Factors in Computing Systems (CHI EA '15)*. Association for Computing Machinery, New York, NY, USA, 687–694. doi:10.1145/2702613.2702969

[25] Yu Jiang, Alice C Haynes, Narjes Pourjafarian, Jan Borchers, and Jürgen Steimle. 2024. Embrogami: Shape-Changing Textiles with Machine Embroidery. In *Proceedings of the 37th Annual ACM Symposium on User Interface Software and Technology (UIST '24)*. Association for Computing Machinery, New York, NY, USA, 1–15. doi:10.1145/3654777.3676431

[26] Ziyuan Jiang, Takafumi Morita, Kanon Aoyama, Yu Kuwajima, Naoki Hosoya, Shingo Maeda, and Yasuaki Kakehi. 2023. A Method for Controlling the Continuous Transparency of Three-dimensional Objects Utilizing Mechanical Emulsification. In *Proceedings of the Seventeenth International Conference on Tangible, Embedded, and Embodied Interaction (TEI '23)*. Association for Computing Machinery, New York, NY, USA, 1–6. doi:10.1145/3569009.3573122

[27] Yuhua Jin, Isabel Qamar, Michael Wessely, Aradhana Adhikari, Katarina Bulovic, Parinya Punpongsanon, and Stefanie Mueller. 2019. Photo-Chromeleon: Re-Programmable Multi-Color Textures Using Photochromic Dyes. In *Proceedings of the 32nd Annual ACM Symposium on User Interface Software and Technology*. ACM, New Orleans LA USA, 701–712. doi:10.1145/3332165.3347905

[28] Alexander Kalus, Johannes Klein, Tien-Julian Ho, Lee-Ann Seegets, and Niels Henze. 2024. MobileGravity: Mobile Simulation of a High Range of Weight in Virtual Reality. In *Proceedings of the 2024 CHI Conference on Human Factors in Computing Systems (CHI '24)*. Association for Computing Machinery, New York, NY, USA, 1–13. doi:10.1145/3613904.3642658

[29] Alexander Kalus, Martin Kocur, Johannes Klein, Manuel Mayer, and Niels Henze. 2023. PumpVR: Rendering the Weight of Objects and Avatars through Liquid Mass Transfer in Virtual Reality. In *Proceedings of the 2023 CHI Conference on Human Factors in Computing Systems (CHI '23)*. Association for Computing Machinery, New York, NY, USA, 1–13. doi:10.1145/3544548.3581172

[30] Hsin-Liu (Cindy) Kao, Christian Holz, Asta Roseway, Andres Calvo, and Chris Schmandt. 2016. DuoSkin: rapidly prototyping on-skin user interfaces using skin-friendly materials. In *Proceedings of the 2016 ACM International Symposium on Wearable Computers (ISWC '16)*. Association for Computing Machinery, New York, NY, USA, 16–23. doi:10.1145/2971763.2971777

[31] Hyunyoung Kim, Aluna Everitt, Carlos Tejada, Mengyu Zhong, and Daniel Ashbrook. 2021. MorpheesPlug: A Toolkit for Prototyping Shape-Changing Interfaces. In *Proceedings of the 2021 CHI Conference on Human Factors in Computing Systems (CHI '21)*. Association for Computing Machinery, New York, NY, USA, 1–13. doi:10.1145/3411764.3445786

[32] Pin-Sung Ku, Kunpeng Huang, and Cindy Hsin-Liu Kao. 2022. Patch-O: Deformable Woven Patches for On-body Actuation. In *Proceedings of the 2022 CHI Conference on Human Factors in Computing Systems (CHI '22)*. Association for Computing Machinery, New York, NY, USA, 1–12. doi:10.1145/3491102.3517633

[33] Pin-Sung Ku, Shuwen Jiang, Wei-Hsin Wang, and Hsin-Liu Cindy Kao. 2024. ECSkin: Tessellating Electrochromic Films for Reconfigurable On-skin Displays. *Proc. ACM Interact. Mob. Wearable Ubiquitous Technol.* 8, 2 (May 2024), 60:1–60:26. doi:10.1145/3659613

[34] Edouard Leroy and Herbert Shea. [n. d.]. Hydraulically Amplified Electrostatic Taxels (HAXELs) for Full Body Haptics. ([n. d.]). doi:10.1002/admt.202300242

[35] Guanhong Liu, Haiqing Xu, Xianghua(Sharon) Ding, Mingyue Gao, Bowen Li, Fushen Ruan, and Haipeng Mi. 2022. "It Puts Life into My Creations": Understanding Fluid Fiber as a Media for Expressive Display. In *Proceedings of the 2022 CHI Conference on Human Factors in Computing Systems (CHI '22)*. Association for Computing Machinery, New York, NY, USA. doi:10.1145/3491102.3501990 event-place: New Orleans, LA, USA.

[36] Yuhu Liu, Satoshi Nishikawa, Young ah Seong, Ryuma Niiyama, and Yasuo Kuniyoshi. 2021. ThermoCaress: A Wearable Haptic Device with Illusory Moving Thermal Stimulation. In *Proceedings of the 2021 CHI Conference on Human Factors in Computing Systems (CHI '21)*. Association for Computing Machinery, New York, NY, USA. doi:10.1145/3411764.3445777 event-place: Yokohama, Japan.

[37] Jasmine Lu, Ziwei Liu, Jas Brooks, and Pedro Lopes. 2021. Chemical Haptics: Rendering Haptic Sensations via Topical Stimulants. In *The 34th Annual ACM*

Symposium on User Interface Software and Technology. ACM, Virtual Event USA, 239–257. doi:10.1145/3472749.3474747

[38] Qiuyu Lu, Jifei Ou, João Wilbert, André Haben, Haipeng Mi, and Hiroshi Ishii. 2019. milliMorph – Fluid-Driven Thin Film Shape-Change Materials for Interaction Design. In *Proceedings of the 32nd Annual ACM Symposium on User Interface Software and Technology*. ACM, New Orleans LA USA, 663–672. doi:10.1145/3332165.3347956

[39] Yiyue Luo, Junyi Zhu, Kui Wu, Cedric Honnet, Stefanie Mueller, and Wojciech Matusik. 2023. MagKnitic: Machine-knitted Passive and Interactive Haptic Textiles with Integrated Binary Sensing. In *Proceedings of the 36th Annual ACM Symposium on User Interface Software and Technology (UIST '23)*. Association for Computing Machinery, New York, NY, USA, 1–13. doi:10.1145/3586183.3606765

[40] Eric Markvicka, Guanyun Wang, Yi-Chin Lee, Gierad Laput, Carmel Majidi, and Lining Yao. 2019. ElectroDermis: Fully Untethered, Stretchable, and Highly-Customizable Electronic Bandages. In *Proceedings of the 2019 CHI Conference on Human Factors in Computing Systems (CHI '19)*. Association for Computing Machinery, New York, NY, USA, 1–10. doi:10.1145/3290605.3300862

[41] Alex Mazursky, Jacob Serfaty, and Pedro Lopes. 2024. Stick&Slip: Altering Fingerpad Friction via Liquid Coatings. In *Proceedings of the 2024 CHI Conference on Human Factors in Computing Systems (CHI '24)*. Association for Computing Machinery, New York, NY, USA, 1–14. doi:10.1145/3613904.3642299

[42] Hila Mor, Tianyu Yu, Ken Nakagaki, Benjamin Harvey Miller, Yichen Jia, and Hiroshi Ishii. 2020. Venous Materials: Towards Interactive Fluidic Mechanisms. In *Proceedings of the 2020 CHI Conference on Human Factors in Computing Systems*. ACM, Honolulu HI USA, 1–14. doi:10.1145/3313831.3376129

[43] Takafumi Morita and Yasuaki Kakehi. 2023. see-saw: A Kinetic Installation that Unfolds in Silence Driven by Liquid Flow. In *SIGGRAPH Asia 2023 Art Papers (SA '23)*. Association for Computing Machinery, New York, NY, USA, 1–6. doi:10.1145/3610591.3616434

[44] Takafumi Morita, Yu Kuwajima, Ayato Minaminosono, Shingo Maeda, and Yasuaki Kakehi. 2022. HydroMod : Constructive Modules for Prototyping Hydraulic Physical Interfaces. In *CHI Conference on Human Factors in Computing Systems*. ACM, New Orleans LA USA, 1–14. doi:10.1145/3491102.3502096

[45] Jifei Ou, Mélina Skouras, Nikolaos Vlavianos, Felix Heibeck, Chin-Yi Cheng, Jannik Peters, and Hiroshi Ishii. 2016. aeroMorph - Heat-sealing Inflatable Shape-change Materials for Interaction Design. In *Proceedings of the 29th Annual Symposium on User Interface Software and Technology (UIST '16)*. Association for Computing Machinery, New York, NY, USA, 121–132. doi:10.1145/2984511.2984520

[46] Roshan Lalitha Peiris, Yuan-Ling Feng, Liwei Chan, and Kouta Minamizawa. 2019. ThermalBracelet: Exploring Thermal Haptic Feedback Around the Wrist. In *Proceedings of the 2019 CHI Conference on Human Factors in Computing Systems*. ACM, Glasgow Scotland Uk, 1–11. doi:10.1145/3290605.3300400

[47] Purnendu, Sasha M Novack, Eric Acome, Christoph Keplinger, Mirela Alistar, Mark D Gross, Carson Bruns, and Daniel Leithinger. 2021. Electriflow: Soft Electrohydraulic Building Blocks for Prototyping Shape-changing Interfaces. In *Proceedings of the 2021 ACM Designing Interactive Systems Conference (DIS '21)*. Association for Computing Machinery, New York, NY, USA, 1280–1290. doi:10.1145/3461778.3462093

[48] Tucker Rae-Grant, Chris Harrison, and Craig Shultz. 2024. DynaButtons: Fast Interactive Soft Buttons with Analog Control. In *2024 IEEE Haptics Symposium (HAPTICS)*. 366–371. doi:10.1109/HAPTICS59260.2024.10520864 ISSN: 2324-7355.

[49] Philipp Rothemund, Nicholas Kellaris, Shane K. Mitchell, Eric Acome, and Christoph Keplinger. 2021. HASEL Artificial Muscles for a New Generation of Lifelike Robots—Recent Progress and Future Opportunities. *Advanced Materials* 33, 19 (2021), 2003375. doi:10.1002/adma.202003375 _eprint: https://onlinelibrary.wiley.com/doi/pdf/10.1002/adma.202003375.

[50] Natalia Sanchez-Tamayo, Zachary Yoder, Philipp Rothemund, Giulia Ballardini, Christoph Keplinger, and Katherine J. Kuchenbecker. [n. d.]. Cutaneous Electrohydraulic (CUTE) Wearable Devices for Pleasant Broad-Bandwidth Haptic Cues. *Advanced Science* n/a, n/a ([n. d.]), 2402461. doi:10.1002/advs.202402461 _eprint: https://onlinelibrary.wiley.com/doi/pdf/10.1002/advs.202402461.

[51] Ticha Sethapakdi, Laura Huang, Vivian Hsinyueh Chan, Lung-Pan Cheng, Fernando Fuzinatto Dall'Agnol, Mackenzie Leake, and Stefanie Mueller. 2023. Polagons: Designing and Fabricating Polarized Light Mosaics with User-Defined Color-Changing Behaviors. In *Proceedings of the 2023 CHI Conference on Human Factors in Computing Systems (CHI '23)*. Association for Computing Machinery, New York, NY, USA, 1–14. doi:10.1145/3544548.3580639

[52] Ticha Sethapakdi, Paris Myers, Tianyu Yu, Juliana Covarrubias, Mackenzie Leake, and Stefanie Mueller. 2024. Thermochromorph: Dynamic Relief Printing with Thermochromic Inks. In *SIGGRAPH Asia 2024 Art Papers (SA '24)*. Association for Computing Machinery, New York, NY, USA, 1–7. doi:10.1145/3680530.3695445

[53] Vivian Shen, Tucker Rae-Grant, Joe Mullenbach, Chris Harrison, and Craig Shultz. 2023. Fluid Reality: High-Resolution, Untethered Haptic Gloves using Electroosmotic Pump Arrays. In *Proceedings of the 36th Annual ACM Symposium on User Interface Software and Technology (UIST '23)*. Association for Computing Machinery, New York, NY, USA, 1–20. doi:10.1145/3586183.3606771

[54] Ali Shtarbanov. 2021. FlowIO Development Platform – the Pneumatic "Raspberry Pi" for Soft Robotics. In *Extended Abstracts of the 2021 CHI Conference on Human Factors in Computing Systems (CHI EA '21)*. Association for Computing Machinery, New York, NY, USA, 1–6. doi:10.1145/3411763.3451513

[55] Craig Shultz and Chris Harrison. 2023. Flat Panel Haptics: Embedded Electroosmotic Pumps for Scalable Shape Displays. In *Proceedings of the 2023 CHI Conference on Human Factors in Computing Systems (CHI '23)*. Association for Computing Machinery, New York, NY, USA, 1–16. doi:10.1145/3544548.3581547

[56] Katherine Wei Song, Christine Dierk, Szu Ting Tung, and Eric Paulos. 2023. Lotio: Lotion-Mediated Interaction with an Electronic Skin-Worn Display. In *Proceedings of the 2023 CHI Conference on Human Factors in Computing Systems (CHI '23)*. Association for Computing Machinery, New York, NY, USA, 1–15. doi:10.1145/3544548.3581098

[57] Wei Sun, Yuwen Chen, Yanjun Chen, Xiaopeng Zhang, Simon Zhan, Yixin Li, Jiecheng Wu, Teng Han, Haipeng Mi, Jingxian Wang, Feng Tian, and Xing-Dong Yang. 2022. MicroFluID: A Multi-Chip RFID Tag for Interaction Sensing Based on Microfluidic Switches. *Proceedings of the ACM on Interactive, Mobile, Wearable and Ubiquitous Technologies* 6, 3 (2022), 141:1–141:23. doi:10.1145/3550296

[58] Saya Suzunaga, Yuichi Itoh, Yuki Inoue, Kazuyuki Fujita, and Takao Onoye. 2020. TuVe: A Shape-changeable Display using Fluids in a Tube. In *Proceedings of the 2020 International Conference on Advanced Visual Interfaces (AVI '20)*. Association for Computing Machinery, New York, NY, USA, 1–9. doi:10.1145/3399715.3399874

[59] Yudai Tanaka, Alan Shen, Andy Kong, and Pedro Lopes. 2023. Full-hand Electro-Tactile Feedback without Obstructing Palmar Side of Hand. In *Proceedings of the 2023 CHI Conference on Human Factors in Computing Systems (CHI '23)*. Association for Computing Machinery, New York, NY, USA, 1–15. doi:10.1145/3544548.3581382

[60] Wei Tang, Yiding Zhong, Huxiu Xu, Kecheng Qin, Xinyu Guo, Yu Hu, Pingan Zhu, Yang Qu, Dong Yan, Zhaoyang Li, Zhongdong Jiao, Xujun Fan, Huayong Yang, and Jun Zou. 2023. Self-protection soft fluidic robots with rapid large-area self-healing capabilities. *Nature Communications* 14, 1 (Oct. 2023), 6430. doi:10.1038/s41467-023-42214-5 Publisher: Nature Publishing Group.

[61] Cesar Torres, Jasper O'Leary, Molly Nicholas, and Eric Paulos. 2017. Illumination Aesthetics: Light as a Creative Material within Computational Design. In *Proceedings of the 2017 CHI Conference on Human Factors in Computing Systems*. ACM, Denver Colorado USA, 6111–6122. doi:10.1145/3025453.3025466

[62] Anusha Withana, Daniel Groeger, and Jürgen Steimle. 2018. Tacttoo: A Thin and Feel-Through Tattoo for On-Skin Tactile Output. In *Proceedings of the 31st Annual ACM Symposium on User Interface Software and Technology (UIST '18)*. Association for Computing Machinery, New York, NY, USA, 365–378. doi:10.1145/3242587.3242645

[63] Te-Yen Wu, Lu Tan, Yuji Zhang, Teddy Seyed, and Xing-Dong Yang. 2020. Capacitivo: Contact-Based Object Recognition on Interactive Fabrics using Capacitive Sensing. In *Proceedings of the 33rd Annual ACM Symposium on User Interface Software and Technology (UIST '20)*. Association for Computing Machinery, New York, NY, USA, 649–661. doi:10.1145/3379337.3415829

[64] Zeyu Yan and Huaishu Peng. 2021. FabHydro: Printing Interactive Hydraulic Devices with an Affordable SLA 3D Printer. In *The 34th Annual ACM Symposium on User Interface Software and Technology (UIST '21)*. Association for Computing Machinery, New York, NY, USA, 298–311. doi:10.1145/3472749.3474751 event-place: Virtual Event, USA.

[65] Willa Yunqi Yang, Yifan Zou, Jingle Huang, Raouf Abujaber, and Ken Nakagaki. 2024. TorqueCapsules: Fully-Encapsulated Flywheel Actuation Modules for Designing and Prototyping Movement-Based and Kinesthetic Interaction. In *Proceedings of the 37th Annual ACM Symposium on User Interface Software and Technology (UIST '24)*. Association for Computing Machinery, New York, NY, USA, 1–15. doi:10.1145/3654777.3676364

[66] Lining Yao, Ryuma Niiyama, Jifei Ou, Sean Follmer, Clark Della Silva, and Hiroshi Ishii. 2013. PneUI: Pneumatically Actuated Soft Composite Materials for Shape Changing Interfaces. In *Proceedings of the 26th Annual ACM Symposium on User Interface Software and Technology (UIST '13)*. Association for Computing Machinery, New York, NY, USA, 13–22. doi:10.1145/2501988.2502037 event-place: St. Andrews, Scotland, United Kingdom.

[67] Lining Yao, Jifei Ou, Chin-Yi Cheng, Helene Steiner, Wen Wang, Guanyun Wang, and Hiroshi Ishii. 2015. bioLogic: Natto Cells as Nanoactuators for Shape Changing Interfaces. In *Proceedings of the 33rd Annual ACM Conference on Human Factors in Computing Systems (CHI '15)*. Association for Computing Machinery, New York, NY, USA, 1–10. doi:10.1145/2702123.2702611

[68] Zachary Yoder, Ellen H. Rumley, Ingemar Schmidt, Philipp Rothemund, and Christoph Keplinger. 2024. Hexagonal electrohydraulic modules for rapidly reconfigurable high-speed robots. *Science Robotics* 9, 94 (Sept. 2024), eadl3546. doi:10.1126/scirobotics.adl3546 Publisher: American Association for the Advancement of Science.

[69] Tianyu Yu, Yige Fan, Zhixiang Zhang, Qingyu Hu, Weiye Xu, Haipeng Mi, and Stefanie Mueller. 2024. Thermaterial: Program Ambient Heat Transfer Behaviors on Objects through Fluidic Composites. In *Extended Abstracts of the 2024 CHI Conference on Human Factors in Computing Systems (CHI EA '24)*. Association for Computing Machinery, New York, NY, USA, 1–8. doi:10.1145/3613905.3650747

[70] Tianyu Yu, Yang Liu, Yujia Liu, Qiuyu Lu, Teng Han, and Haipeng Mi. 2024. FlexEOP: Flexible Shape-changing Actuator using Embedded Electroosmotic

Pumps. In *Adjunct Proceedings of the 37th Annual ACM Symposium on User Interface Software and Technology (UIST Adjunct '24)*. Association for Computing Machinery, New York, NY, USA, 1–5. doi:10.1145/3672539.3686785

[71] Tianyu Yu, Mengjia Niu, Haipeng Mi, and Qiuyu Lu. 2024. MilliWare: Parametric Modeling and Simulation of Millifluidic Shape-changing Interface. In *Proceedings of the Eleventh International Symposium of Chinese CHI (CHCHI '23)*. Association for Computing Machinery, New York, NY, USA, 461–467. doi:10.1145/3629606.3629654

[72] Tianyu Yu, Weiye Xu, Haiqing Xu, Guanhong Liu, Chang Liu, Guanyun Wang, and Haipeng Mi. 2023. Thermotion: Design and Fabrication of Thermofluidic Composites for Animation Effects on Object Surfaces. In *Proceedings of the 2023 CHI Conference on Human Factors in Computing Systems (CHI '23)*. Association for Computing Machinery, New York, NY, USA, 1–19. doi:10.1145/3544548.3580743

[73] Tianhong Catherine Yu, Riku Arakawa, James McCann, and Mayank Goel. 2023. uKnit: A Position-Aware Reconfigurable Machine-Knitted Wearable for Gestural Interaction and Passive Sensing using Electrical Impedance Tomography. In *Proceedings of the 2023 CHI Conference on Human Factors in Computing Systems (CHI '23)*. Association for Computing Machinery, New York, NY, USA, 1–17. doi:10.1145/3544548.3580692

[74] Tianhong Catherine Yu, Manru Mary Zhang, Peter He, Chi-Jung Lee, Cassidy Cheesman, Saif Mahmud, Ruidong Zhang, Francois Guimbretiere, and Cheng Zhang. 2024. SeamPose: Repurposing Seams as Capacitive Sensors in a Shirt for Upper-Body Pose Tracking. In *Proceedings of the 37th Annual ACM Symposium on User Interface Software and Technology (UIST '24)*. Association for Computing Machinery, New York, NY, USA, 1–13. doi:10.1145/3654777.3676341

[75] Junyi Zhu, Yuxuan Lei, Aashini Shah, Gila Schein, Hamid Ghaednia, Joseph Schwab, Casper Harteveld, and Stefanie Mueller. 2022. MuscleRehab: Improving Unsupervised Physical Rehabilitation by Monitoring and Visualizing Muscle Engagement. In *Proceedings of the 35th Annual ACM Symposium on User Interface Software and Technology (UIST '22)*. Association for Computing Machinery, New York, NY, USA, 1–14. doi:10.1145/3526113.3545705